

## REX

Curtis, N.; Walshe, J.

DOI:

[10.1016/j.nima.2015.06.027](https://doi.org/10.1016/j.nima.2015.06.027)

License:

Creative Commons: Attribution-NonCommercial-NoDerivs (CC BY-NC-ND)

*Document Version*

Peer reviewed version

*Citation for published version (Harvard):*

Curtis, N & Walshe, J 2015, 'REX: a Monte Carlo simulation of thick gas target resonant scattering reactions', *Nuclear Instruments & Methods in Physics Research. Section A. Accelerators, Spectrometers, Detectors*, vol. 797, pp. 44-56. <https://doi.org/10.1016/j.nima.2015.06.027>

[Link to publication on Research at Birmingham portal](#)

### **Publisher Rights Statement:**

Eligibility for repository: Checked on 14/09/2015

### **General rights**

Unless a licence is specified above, all rights (including copyright and moral rights) in this document are retained by the authors and/or the copyright holders. The express permission of the copyright holder must be obtained for any use of this material other than for purposes permitted by law.

- Users may freely distribute the URL that is used to identify this publication.
- Users may download and/or print one copy of the publication from the University of Birmingham research portal for the purpose of private study or non-commercial research.
- User may use extracts from the document in line with the concept of 'fair dealing' under the Copyright, Designs and Patents Act 1988 (?)
- Users may not further distribute the material nor use it for the purposes of commercial gain.

Where a licence is displayed above, please note the terms and conditions of the licence govern your use of this document.

When citing, please reference the published version.

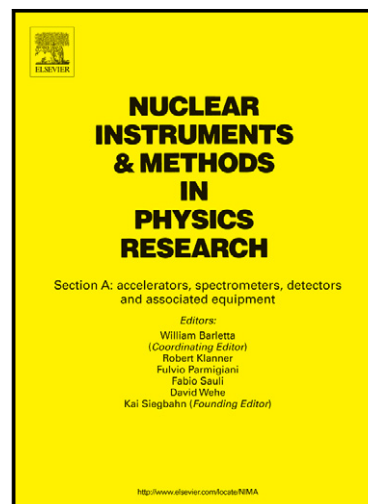
### **Take down policy**

While the University of Birmingham exercises care and attention in making items available there are rare occasions when an item has been uploaded in error or has been deemed to be commercially or otherwise sensitive.

If you believe that this is the case for this document, please contact [UBIRA@lists.bham.ac.uk](mailto:UBIRA@lists.bham.ac.uk) providing details and we will remove access to the work immediately and investigate.

REX: A Monte Carlo simulation of thick gas target resonant scattering reactions

N. Curtis, J. Walshe



[www.elsevier.com/locate/nima](http://www.elsevier.com/locate/nima)

PII: S0168-9002(15)00777-9

DOI: <http://dx.doi.org/10.1016/j.nima.2015.06.027>

Reference: NIMA57828

To appear in: *Nuclear Instruments and Methods in Physics Research A*

Received date: 15 April 2015

Revised date: 11 June 2015

Accepted date: 15 June 2015

Cite this article as: N. Curtis, J. Walshe, REX: A Monte Carlo simulation of thick gas target resonant scattering reactions, *Nuclear Instruments and Methods in Physics Research A*, <http://dx.doi.org/10.1016/j.nima.2015.06.027>

This is a PDF file of an unedited manuscript that has been accepted for publication. As a service to our customers we are providing this early version of the manuscript. The manuscript will undergo copyediting, typesetting, and review of the resulting galley proof before it is published in its final citable form. Please note that during the production process errors may be discovered which could affect the content, and all legal disclaimers that apply to the journal pertain.

# REX: A Monte Carlo simulation of thick gas target resonant scattering reactions

N. Curtis<sup>a,\*</sup>, J. Walshe<sup>a</sup>

<sup>a</sup>*School of Physics and Astronomy, University of Birmingham, Edgbaston, Birmingham,  
B15 2TT, UK*

---

## Abstract

A Monte Carlo code has been developed to simulate resonant scattering reactions using the thick gas target technique in inverse kinematics. Results are presented for the  ${}^4\text{He}({}^{20}\text{Ne},\alpha){}^{20}\text{Ne}$  reaction at 70 MeV, and compared to an experimental measurement which utilised an array of segmented silicon strip detectors. In the case studied, angular straggling in the chamber window is found to dominate the excitation energy resolution.

*Keywords:*

Monte Carlo, Inverse kinematics, Thick target, Resonant scattering

*PACS:* 21.10.-k, 24.10.Lx, 24.30.-v, 25.55.-e

---

## 1. Introduction

The technique of thick target resonant scattering provides an extremely useful tool in the study of  $\alpha$ -cluster states [1], and has been used in a number of experiments in recent years (see, for example, [2–12]). In this method the scattering chamber is de-coupled from the beam line using a thin window (typically Mylar<sup>®</sup> or Havar<sup>®</sup>), and filled with He gas. The He gas acts as both the reaction target and an absorber to slow (and stop) the incoming beam. In this way several resonances may be studied simultaneously with a single beam energy, as the energy loss of the beam in the gas will result in a reduction in the excitation energy with distance into the chamber. This is in contrast to a more traditional thin target experimental setup, where many beam energies are required to produce an excitation function.

---

*Preprint submitted to Nuclear Instruments and Methods A*  
Corresponding author. E-mail address: n.curtis@bham.ac.uk (N. Curtis)

June 18, 2015

Figure 1: (Colour online) Schematic chamber setup of a thick gas target resonant scattering experiment.

If the gas thickness and/or pressure is sufficiently high, and the beam heavier than  $^4\text{He}$  (so that the beam stops in the gas before the scattered  $^4\text{He}$  recoils), detectors may be placed on the beam axis (at  $0^\circ$ ) inside the gas volume to detect the recoiling  $\alpha$ -particles, without being damaged by the beam. This allows reactions to be studied at  $180^\circ$  (in the centre-of-mass (CM) frame), an angle where the non-resonant cross-section is typically much lower than the resonant cross-section, allowing  $\alpha$ -cluster states to be easily distinguished [1]. Detectors placed away from  $0^\circ$  allow  $\alpha$ -particle angular distributions to be studied, providing spin information for the resonances.

A schematic diagram of a typical chamber setup used in a thick gas target resonant scattering experiment is shown in Fig. 1 (the detectors labelled DSSD and LAMP are described in Section 3). The incoming beam will pass through the thin window separating the vacuum tube and the He filled chamber, and begin to lose energy in the gas. At some distance into the chamber the beam will interact with a He nucleus and form a resonance in the compound system. This resonance will subsequently decay, most likely back into the beam species and an  $\alpha$ -particle. For example, in the case of the  $^4\text{He}(^{20}\text{Ne},\alpha)^{20}\text{Ne}$  reaction studied in this work, the  $^4\text{He}$  and  $^{20}\text{Ne}$  form a resonance in the compound nucleus  $^{24}\text{Mg}$ ,

46 before decaying back into a  $^{20}\text{Ne}$  nucleus and an  $\alpha$ -particle. Usually it is only the  
 47 recoiling  $\alpha$ -particle that is detected, as the heavier scattered beam experiences  
 48 greater energy loss and tends to stop before reaching the detectors. In the  
 49 case of the  $^4\text{He}(^6\text{He},\alpha)^6\text{He}$  reaction studied in [2], however, it was possible to  
 50 detect both the  $^6\text{He}$  and  $\alpha$ -particle in coincidence, due to the relatively low mass  
 51 and charge of the  $^6\text{He}$ . A coincidence measurement is typically cleaner than a  
 52 singles experiment, as the need for explicit particle identification is removed  
 53 (particle identification being easily obtained from the particle energy and two-  
 54 body kinematics). In the case of the  $^4\text{He}(^{20}\text{Ne},\alpha)^{20}\text{Ne}$  reaction studied here,  
 55 particle identification was also not an issue, as the detectors were placed (see  
 56 below) at such a distance that the  $^{20}\text{Ne}$  was always stopped in the gas. Hence  
 57 the assumption that any hit was an  $\alpha$ -particle was generally good (the cross-  
 58 section for decay of the resonant  $^{24}\text{Mg}$  to an exit channel other than  $\alpha + ^{20}\text{Ne}$   
 59 being small).

60 In some reactions it is possible that particles other than recoiling  $\alpha$ -particles  
 61 may be detected. For example, in the  $^4\text{He} + ^{14}\text{O}$  study of [3], a large background  
 62 of protons was seen (the  $^4\text{He}(^{14}\text{O},\text{p})^{17}\text{F}$  reaction has a positive Q-value of + 1.19  
 63 MeV). In this experiment time of flight techniques were used to give particle  
 64 identification, making use of the pulsed nature of the cyclotron beam employed  
 65 in the measurement. This allowed lower energy  $\alpha$ -particles to be detected than  
 66 would have been the case if a  $\Delta\text{E}$ -E telescope had been employed (as was the  
 67 case in, for example, [11]). The particle identification techniques of time of  
 68 flight,  $\Delta\text{E}$ -E energy loss and pulse shape discrimination, may also be required in  
 69 experiments utilising a window with a large hydrogen content (such as Mylar<sup>®</sup>  
 70 or Kevlar<sup>®</sup>), the use of which will most likely produce a significant flux of  
 71 protons liberated from the window material. Scattering of the beam from the  
 72 window (as opposed to the He gas) to detectors placed away from  $0^\circ$  can be  
 73 removed by using a collimator placed inside the gas volume. Such a collimator  
 74 was used to reduce background from scattered beam in the LAMP array used  
 75 in the  $^4\text{He} + ^6\text{He}$  measurement of [2], for example.

76 The thick target resonant scattering technique uses inverse kinematics, and

is therefore especially useful in studying reactions that would otherwise require a radioactive target (such as, for example,  $^{10}\text{Be}$  in the case of [11] or  $^{14}\text{C}$  in the case of [12]), a gas target (such as in the  $^4\text{He} + ^{36}\text{Ar}$  reaction studied in [8]), or both (the  $^4\text{He} + ^6\text{He}$  [2] and  $^4\text{He} + ^{14}\text{O}$  [3] reactions, for example, can in fact only be measured using inverse kinematics, due to the 800 ms half-life of  $^6\text{He}$  and 70.6 s half-life of  $^{14}\text{O}$ ). However, determining the experimental resolution and detection efficiency of such measurements can be challenging, due to the large variation in position of the interaction point within the chamber, and hence the need to track the beam and outgoing particles through the gas. The use of detector arrays with complicated geometry (such as that illustrated in Fig. 1) is an additional problem.

One technique that is ideally suited to modelling thick target resonant scattering experiments is that of Monte Carlo simulation. Simulations can be performed using either general purpose codes, such as GEANT4 [13], or custom codes used for specific fields of research, such as cluster breakup [14], nuclear astrophysics [15] and Coulomb dissociation [16]. Monte Carlo codes have been used to model a wide range of detection systems, ranging from  $\beta$ -decay detectors (for example [17, 18]), neutron arrays (for example [19, 20]) and semiconductor Ge detectors (for example [21, 22]). This paper reports on a new Monte Carlo simulation that has been written to aid both the planning of thick gas target resonant scattering experiments, and to help in the interpretation of the data obtained.

## 2. Monte Carlo simulation code REX

The Monte Carlo code REX (Resonant EXcitation simulation) is written in Fortran, and generates pseudo-events in a form that may be analysed using the same analysis codes as used for real experimental data. This allows a direct comparison between any simulated and experimental spectra of interest, aiding the analysis of real data and the interpretation of results.

At the start of each simulated event REX randomly chooses an excitation

energy ( $E_x$ ) for the scattering interaction from within a user defined distribution (either a uniform distribution or a series of one or more Gaussian line shapes of user defined energy, Full Width at Half Maximum (FWHM) and relative strength). After making an allowance for the beam energy spread, beam divergence, beam spot size, beam steering (offset away from the centre of the beam line) and window, three main processes are simulated as the beam is tracked through the chamber. The first is energy loss ( $\Delta E$ ), which is calculated using a subroutine version of the code DEDX [23]. The second effect is energy straggling ( $E_{strag}$ ), which is simulated by adding a randomly chosen energy to that of the beam. This random energy is chosen from within a Gaussian distribution (centred at zero) of width given by the formalism of Clarke [24]. The third process is angular straggling ( $\theta_{strag}$ ). This is similar to energy straggling, in that randomly chosen angles are added to both the in-plane ( $\theta_x$ ) and out-of-plane ( $\theta_y$ ) angles of the beam. These random angles are chosen from a Gaussian distribution (again centred at zero) of width determined from the multiple scattering equations of Marion and Zimmerman [25]. The effects of energy and angular straggling are therefore to smear the energy and angles of the beam by random (and energy dependent) amounts.

After determining the effects of energy loss, energy straggling and angular straggling in the window, the beam is tracked through the gas in user defined steps. At the end of each step  $\Delta E$ ,  $E_{strag}$  and  $\theta_{strag}$  are calculated for that step, allowing the energy, Cartesian (X, Y, Z) coordinates of the beam particle (the origin being defined as the centre of the window) and the distance to the window to be calculated. The absolute particle in-plane ( $\theta_x$ ) and out-of-plane ( $\theta_y$ ) angles are also determined, as are those relative to the centre of the window. From these the polar ( $\theta$ ) and azimuthal ( $\phi$ ) angles can also be determined. The absolute polar angle ( $\theta_{abs}$ ) and that relative to the window ( $\theta_{win}$ ) are illustrated in Fig. 1. Hence at the end of each step the energy, position within the chamber and direction of travel of the beam particle are known.

The tracking of the beam continues until the energy loss is such that the initially chosen  $E_x$  has been reached. At this point the scattering is simulated,

with the CM scattering angle being chosen from either a uniform, Rutherford or Legendre Polynomial distribution. The energies of the outgoing particles are determined from two-body kinematics, and then they are tracked in the same manner as the beam - at the end of each step the effects of  $\Delta E$ ,  $E_{strag}$  and  $\theta_{strag}$  are calculated, and the particle energies, positions and angles (both absolute and with respect to the window) obtained.

Both outgoing particles are tracked until one of four possible outcomes is met: 1) the energy reaches zero and the particle stops in the gas, 2) the particle hits an active region of a detector, 3) the particle hits the non-active frame of a detector (this simulating the shadowing of detectors further from the window by those closer) and 4) the particle reaches a (user defined) maximum distance from the window without stopping or hitting a detector. In event types 1, 3 and 4 the particle does not hit an active region of a detector and is lost. Once a particle has been determined to have hit a detector (event type 2, described below) a check is made to ensure the energy is greater than the detector energy threshold, and then the energy and position of the particle smeared by the detector energy and position resolution. Events in which either one or both of the particles hit a detector are then written to the output file in the form of pseudo-events, ready for analysis.

Three categories of detector may be simulated by REX. Detectors placed on the beam axis (at  $0^\circ$ ) may be either round (such as surface barrier detectors) or rectangular (such as resistive strip or double sided strip detectors). Rectangular detectors may also be placed at any point in the chamber (centred at  $(R, \theta, \phi)$  (in spherical polar coordinates) with respect to the window), with a tilt angle between  $0^\circ$  (perpendicular to the beam axis) and  $90^\circ$  (parallel to the beam axis). The third category of detectors are Micron Semiconductor Ltd [27] type YY1 detectors [28], used to form the “LAMP” array (as shown in Fig. 1 and described in Section 3.1). The dimensions of the active regions of the detectors as well as any surrounding frames are used to determine if a particle has hit or missed the detectors. Any number of missing or broken strips may also be simulated. Detector hits are determined by comparing the angles and distance from the



168 window of the particles at the end of each gas step, with the angular coverage  
 169 and distances of each detector. If the particle angles lie within the range covered  
 170 by a detector strip, a check is made on the relative distance from the window  
 171 of the particle and the detector at that (angular) point. If the particle distance  
 172 ( $R_p$ ) is less than the detector distance ( $R_d$ ), the particle has not yet reached  
 173 the detector, and another gas step simulated. If  $R_p = R_d$  (within a tolerance  
 174 equal to a tenth of the gas step size) the particle is said to have hit the detector.  
 175 If  $R_p > R_d$  the particle has “passed through” the detector. In this case the  
 176 last gas step is undone and a new gas step (equal to half of the previous step)  
 177 simulated. In this way any particle hitting the detector within the active region  
 178 will register a hit. A similar method is used to determine if the particles hit the  
 179 frame surrounding the detector active region.

180 In addition to  $\Delta E$ ,  $E_{strag}$  and  $\theta_{strag}$  in the window and gas, REX can  
 181 also simulate the same effects arising from absorber foils placed in the beam  
 182 (before and/or after the window). The effects of beam energy spread from the  
 183 accelerator, beam divergence and beam spot size, may be simulated by adding  
 184 a random energy, angle or distance (from a Gaussian distribution centred at  
 185 zero) to the beam energy, in-plane and out-of-plane angles and in-plane and  
 186 out-of-plane distances from the window, at the start of each event, respectively.  
 187 Any offset in the beam from the centre of the window can also be simulated.  
 188 The effect of a collimator placed inside the chamber (after the window) may  
 189 be simulated, as can the energy loss, energy straggling and angular straggling  
 190 through a series of  $0^\circ$  silicon detectors forming a  $\Delta E - E$  telescope (as used in,  
 191 for example, [11]). The detector position resolution can take the form of either  
 192 a Gaussian distribution (for resistive strip detectors) or the strip centroid (for  
 193 non-resistive strip detectors such as those used in the LAMP array in [2, 11]). It  
 194 is possible to turn each smearing effect on or off (in any combination), allowing  
 195 the contribution of each to the excitation energy resolution (for example) to be  
 196 studied.

Figure 2: (Colour online) Schematic of a Micron Semiconductor Ltd type YY1 detector.

### 3. Results and discussion

#### 3.1. The ${}^4\text{He}({}^{20}\text{Ne},\alpha){}^{20}\text{Ne}$ reaction

The  ${}^4\text{He}({}^{20}\text{Ne},\alpha){}^{20}\text{Ne}$  reaction has been simulated in order to compare the output of REX to experimental data. The experiment [26] was performed at the GANIL accelerator facility in Caen, France. A 70 MeV  ${}^{20}\text{Ne}$  beam was used in conjunction with a chamber filled to 540 torr with He gas. The window was 4.8  $\mu\text{m}$  Havar<sup>®</sup>. The detector setup consisted of one double sided silicon strip detector (DSSD) (Micron Semiconductor Ltd [27] type W1) and one LAMP [2, 11] array (as shown in Fig. 1). The DSSD was  $(5 \times 5)$  cm<sup>2</sup> in active area, with 16 horizontal 3 mm wide strips on one face and 16 vertical 3 mm strips on the other. This was placed at 0° (on the beam axis) and 360 mm from the window. The LAMP array was constructed from 6 Micron Semiconductor Ltd type YY1 detectors [28], a schematic of which is shown in Fig. 2. Each YY1

Figure 3: (Colour online) Schematic of the LAMP array used in the experiment of [26]. The side view shown at the bottom corresponds to a line through  $\phi = 90^\circ - 270^\circ$  (in the front view, above).

210 detector consists of a  $45^\circ$  wide wedge shaped PCB (with inner and outer radii of  
 211 40 and 145 mm, respectively) and an active silicon region consisting of 16 non-  
 212 resistive 5 mm wide radial strips. The inner strip (labelled 1 in the following  
 213 discussions) has an inner radius of 50 mm, and the outer strip (labelled 16) an  
 214 inner radius of 125 mm. The inner 13 strips cover an absolute azimuthal width of  
 215  $\phi \approx 40^\circ$ , which reduces to  $\approx 36^\circ$ ,  $29^\circ$  and  $19^\circ$  for the outer 3 strips [28]). When  
 216 8 YY1 detectors are placed together they form a flat and completely circular  
 217 ( $360^\circ$ ) annular array, LEDA [28]. With the removal of two detectors a 6 sided  
 218 cone shaped configuration (known as LAMP) can be created, as shown in Figs. 1  
 219 and 3. In the front view of LAMP, shown at the top of Fig. 3, the azimuthal

Parameter	Value	Parameter	Value
Beam energy	70 MeV	Beam energy spread	200 keV
He gas pressure	540 torr	Beam divergence in X	0.5°
Window material	Havar <sup>®</sup>	Beam divergence in Y	0.5°
Window thickness	4.8 $\mu\text{m}$	Beam spot size in X	6.6 mm
LAMP distance	284 mm	Beam spot size in Y	1.6 mm
DSSD distance	360 mm	Detector energy resolution	100 keV
Gas step size	1 mm	Detector energy threshold	1.2 MeV

Table 1: Values for the  $^4\text{He}(^{20}\text{Ne},\alpha)^{20}\text{Ne}$  simulations.

angles of the 6 detector centres can be seen to be 30°, 90°, 150°, 210°, 270°  
 and 330°. In this view the detectors appear foreshortened, as they are tilted  
 towards the beam line (out of the page) by triangular shaped mounting blocks.  
 These can be seen in the side view, taken along the line  $\phi = 90^\circ$  to 270°, which  
 is shown at the bottom of Fig. 3. The mounting blocks hold the YY1 detectors  
 at an angle of 46° (the angle between the detector face and beam axis), and  
 three pairs of such blocks, with a 60° separation, give the 6 sided cone shaped  
 arrangement seen at the top of Fig. 3, and in the chamber schematic shown in  
 Fig. 1. Each of the 6 mounting blocks are attached to a frame, which is used to  
 hold the LAMP array at the correct height with respect to the beam axis. In the  
 $^4\text{He}(^{20}\text{Ne},\alpha)^{20}\text{Ne}$  experiment [26] simulated, the distance along the beam axis  
 from the window to the inner edge of strip 1 (the strip closest to the beam axis)  
 was 284 mm. At this distance the active region of each YY1 detector mounted  
 in the LAMP array covered an azimuthal angle (as seen from the window) of  $\approx$   
 56°.

Additional details of the experimental setup (used as inputs to REX) are  
 given in Tab. 1. The majority of the simulations were performed with a gas  
 step of 1 mm (and hence a detector hit tolerance of 0.1 mm). The effect of  
 varying the gas step and hit tolerance is discussed below.

### 3.2. Resonance Distance

The results of an investigation into the position within the chamber of a series of resonances are presented in Fig. 4. Here the distance from the window is shown for 7 resonances, generated (with equal weighting) in 1 MeV steps, between  $E_x = 11$  and 17 MeV. In the main panel the resonance distance is plotted separately for events detected in the DSSD and the 16 strips of the LAMP array. In the upper panel all events are shown projected together onto the distance axis. The distance of the resonances varies from 34.3 mm from the window for the resonance at  $E_x = 17$  MeV, to 270.4 mm for that at  $E_x = 11$  MeV. Also indicated in Fig. 4 are the distances from the window of the  $0^\circ$  DSSD (360 mm) and the LAMP array. The outer edge of the outer strip (strip 16) of the LAMP array lies at a distance of 228.4 mm from the window (along the beam axis), and the inner edge of the inner strip (strip 1) at 284.0 mm. It can be seen, therefore, that the resonances at  $E_x = 11$  and 12 MeV sit within the cone of the LAMP array. This results in an excitation energy threshold for the LAMP strips. For example, events in which scattering is simulated at  $E_x = 11$  MeV cannot be detected in any of the 16 strips of the LAMP detectors. This is because the  $\alpha$ -particle produced in the  ${}^4\text{He}({}^{20}\text{Ne}, \alpha){}^{20}\text{Ne}$  reaction cannot scatter to large enough angles (due to two-body kinematics) to hit the detectors with sufficient energy to overcome the energy thresholds. In addition, only strips 1 and 2 can detect events from the 12 MeV resonance, and strips 1 – 9 that at  $E_x = 13$  MeV. All 16 strips can detect events generated at  $E_x = 14$  MeV and above. In contrast, and due to its positioning within the chamber, all 7 resonances can be detected in all strips of the  $0^\circ$  DSSD. Such investigations will provide useful information when planning the setup of future experiments.

The resonances shown in Fig. 4 were generated with an excitation energy width of 1 keV. Due to energy straggling of the beam in the window and gas, this translates to a FWHM of approximately 4 mm in position within the chamber. It is necessary, therefore, to use a gas step that is smaller than 4 mm in the simulations, to ensure correct sampling of the resonances. As mentioned previously, the majority of results were obtained with a step size of 1 mm, although

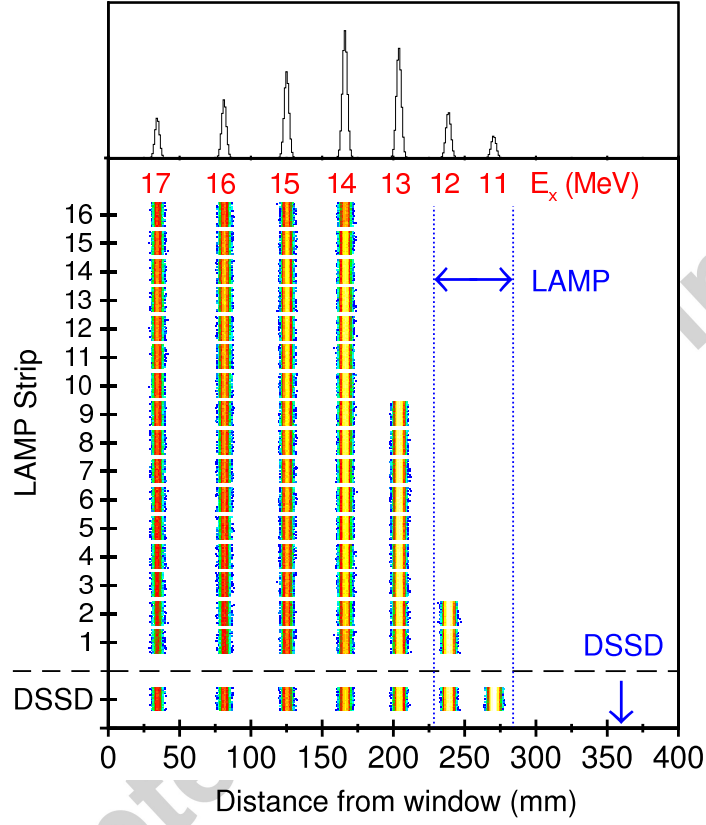


Figure 4: (Colour online) Distance from the window (along the beam axis) for a series of 1 keV wide resonances, generated at  $E_x = 11 - 17$  MeV, as detected in the DSSD and LAMP detectors of [26]. The distance to the  $0^\circ$  DSSD (360 mm) and coverage of the LAMP array (228.4 to 284.0 mm) are indicated. The upper panel shows the projection of all events onto the distance axis.

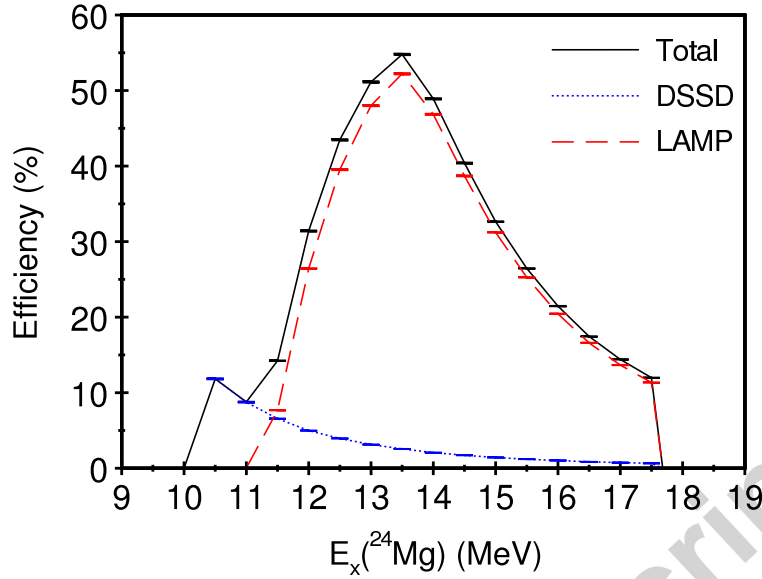


Figure 5: (Colour online) Efficiency profile for the 0° DSSD (blue dotted line), LAMP array (red dashed line) and overall value (black solid line) in the experiment of [26].

steps of 0.1, 0.2, 0.5, 1.5 and 2.0 mm have also been investigated (see below).

### 3.3. Geometrical Detection Efficiency

The geometrical detection efficiency obtained from REX for the experimental setup of [26] is shown in Fig. 5. The maximum excitation energy reached in the experiment is determined by the energy of the beam directly after the window,  $E_x = 17.68$  MeV. The minimum excitation is given by the reaction  $Q$ -value, 9.31 MeV. However, as events occurring at excitation energies close to the reaction  $Q$ -value will produce outgoing particles with very low kinetic energies, in practice this minimum excitation energy is not seen, due to the energy thresholds set on the detector signals to remove noise. Hence the actual detected  $E_x$  range is 10.08 – 17.68 MeV. In Fig. 5 the efficiencies are plotted in 0.5 MeV  $E_x$  steps for both the 0° DSSD detector (blue dotted line) and LAMP array (red dashed line). Also shown is the total efficiency (black solid line). The excitation energy threshold of the LAMP array discussed in Section 3.2 may be seen in Fig. 5,

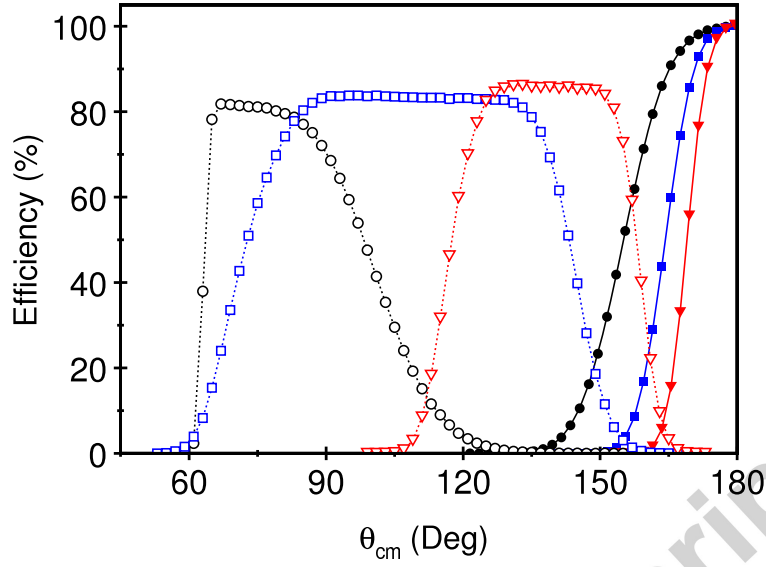


Figure 6: (Colour online) Efficiency profile for the  $0^\circ$  DSSD (solid lines and closed points) and LAMP array (dotted lines and open points) of [26] against CM scattering angle, for excitation energies of 12 (black lines and circles), 14 (blue lines and squares) and 16 (red lines and triangles) MeV.

the LAMP efficiency being zero at 11 MeV. This is in contrast to the  $0^\circ$  DSSD efficiency, which is 8.75 % at this point.

The efficiencies of the  $0^\circ$  DSSD and LAMP array of [26] are shown as a function of CM scattering angle in Fig. 6, for excitation energies of 12, 14 and 16 MeV. The excitation energy threshold of the LAMP array (seen in Fig. 5) also appears in Fig. 6 as a sharp cut-off in the 12 MeV (black dotted line with open circles) distribution at  $\theta_{cm} \sim 60^\circ$ . Despite this, it can clearly be seen that the various distributions become narrower and centred towards larger CM angles, as the excitation energy increases. This is because high  $E_x$  values correspond to smaller distances into the chamber (as seen in Fig. 4) and hence greater distances from the detectors. This in turn leads to a reduction in the solid angles covered by the detectors with respect to the resonance point, and hence a narrowing of the efficiency profiles. The shift to smaller (more forward) laboratory angles arising from this translates as a shift to higher CM angles,



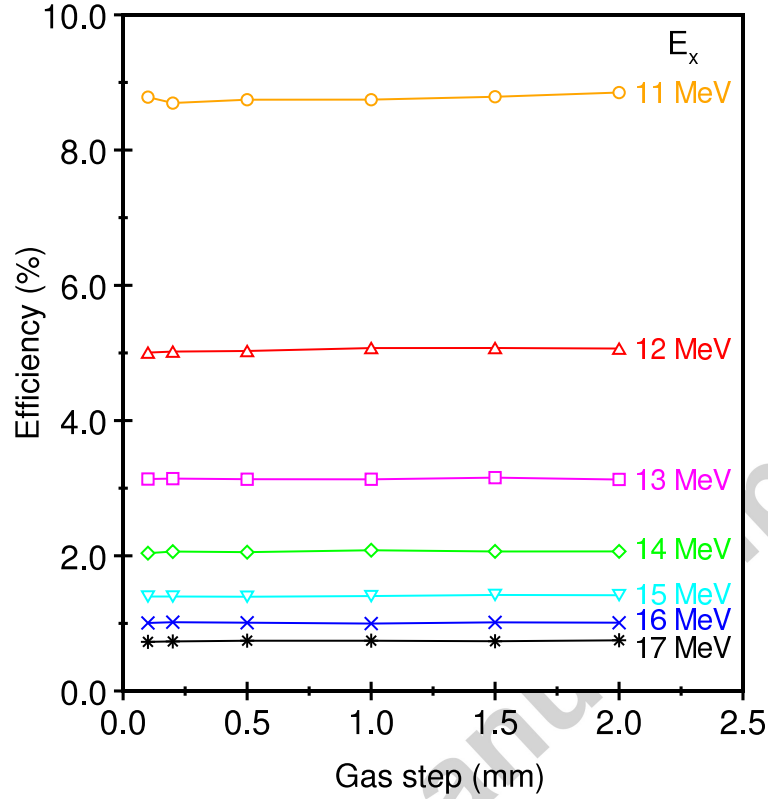


Figure 7: (Colour online) Efficiency for the  $0^\circ$  DSSD of [26] as a function of REX gas step size, for excitation energies of 11 (orange line with circles), 12 (red line with deltas), 13 (magenta line with squares), 14 (green line with diamonds), 15 (cyan line with triangles), 16 (blue line with crosses) and 17 (black line with stars) MeV.

due to the use of inverse kinematics in the reaction. As the  $0^\circ$  DSSD is situated on the beam axis in the scattering chamber, the three DSSD profiles shown in Fig. 6 all reach 100 % efficiency at  $\theta_{cm} = 180^\circ$ . This is in contrast to the LAMP array, which has a maximum efficiency of only 81 – 86 %, a result of the gaps in the azimuthal coverage that arise from the PCB surrounding the silicon on the YY1 detectors.

In Fig. 7 the efficiency of the  $0^\circ$  DSSD is shown as a function of the gas step size used in the REX simulations (0.1, 0.2, 0.5, 1.0, 1.5 and 2.0 mm). Resonances have been simulated at 1 MeV intervals between 11 and 17 MeV. In

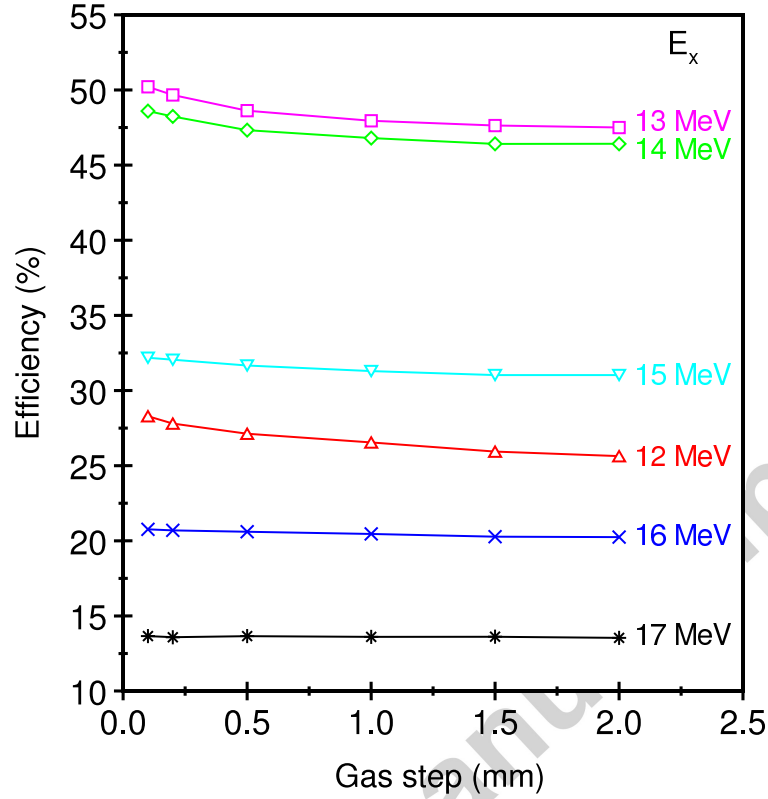


Figure 8: (Colour online) Efficiency for the LAMP array of [26] as a function of REX gas step size, for excitation energies of 12 (red line with deltas), 13 (magenta line with squares), 14 (green line with diamonds), 15 (cyan line with triangles), 16 (blue line with crosses) and 17 (black line with stars) MeV.

all cases the data are independent of the gas step size used, within the statistical fluctuations of the simulations. The uncertainties vary from absolute efficiency values  $\pm 0.05$  % at  $E_x = 11$  MeV, to  $\pm 0.008$  % at  $E_x = 17$  MeV (and as such are too small to be shown in Fig. 7).

The effect of altering the gas step size on the LAMP efficiency is shown in Fig. 8, and a clear dependence may be observed. The greatest effect is seen at  $E_x = 12$  MeV, where the efficiency obtained with a step of 2.0 mm,  $(25.63 \pm 0.07)$  %, increases to  $(28.29 \pm 0.08)$  % for a step of 0.1 mm, an absolute difference of  $\sim 2.7$  %. The variation decreases with increasing excitation energy, however,

so that by  $E_x = 17$  MeV the difference in efficiencies for the 2.0 and 0.1 mm steps,  $(13.54 \pm 0.04) \%$  and  $(13.65 \pm 0.04) \%$  respectively, is only  $\sim 0.1 \%$ . The dependence observed in Fig. 8 results from the sensitivity of the efficiency to the solid angle of the detector strips, which in turn depends on the accuracy to which the position of the resonance can be determined within the chamber. The effect is greatest at  $E_x = 12$  MeV, as this resonance sits within the cone of the LAMP array (as seen in Fig. 4). The effect decreases with increasing excitation energy, as the higher excitation resonances are increasingly further from the LAMP array. While such an effect should also be seen for the  $0^\circ$  DSSD, it is further from the resonances than the LAMP array, and mounted perpendicularly to the beam axis. This reduces the variation in efficiency with gas step (as seen in the tilted detectors of LAMP), to the extent that the effect is not seen in Fig. 7. As the data obtained with LAMP are only used to study angular distributions, and the yield is not required to be efficiency corrected to produce an excitation energy spectrum (in barns), the variation in efficiency with gas step size does not pose a real issue in the analysis of experimental data.

The results shown in Figs. 7 and 8 were obtained by varying the gas step size. This in turn resulted in a variation in the detector hit tolerance (as described in Section 2), as this is set to 10 % of the gas step. Simulations have also been performed with a fixed tolerance of 0.1 mm at all gas steps. The results are the same as those shown in Figs. 7 and 8, and are not presented. These simulations show that the variation in efficiency with gas step size seen in Fig. 8 for the LAMP array is not due to the changing hit tolerance condition.

### 3.4. Resolution

The excitation energy of resonances populated in thick gas target resonant scattering reactions may be obtained from the detected energy,  $E_d$ , of the  $\alpha$ -particle. This requires a simulation of the reaction in which only energy loss effects are considered. A polynomial fit to the distribution of detected energies as a function of the simulated excitation energy, generated with a uniform distribution, allows  $E_x$  to be determined from  $E_d$  on an event by event ba-

sis. To remove any angular effects, a polynomial is obtained for each detector strip, or, in the case of a DSSD, for each of the “pixels” formed by the crossing of one front and one back strip. Once these polynomials have been obtained, the  $E_x$  resolution of the experimental setup may be studied by running further simulations, in which narrow ( $\text{FWHM} = 1 \text{ keV}$ ) resonances are generated. By observing the width with which these resonances are reconstructed in the data analysis, the  $E_x$  resolution may be determined. As each smearing effect can be turned on or off in any combination in REX, the contribution from each to the total  $E_x$  resolution may be obtained.

Fig. 9 shows the excitation energy obtained from the detected  $\alpha$ -particle energy, for a REX simulation of a resonance at 16 MeV, for all of the pixels of the  $0^\circ$  DSSD of [26] added together. In Fig. 9(a) the results of a simulation with all smearing effects turned off (except energy loss in the window and gas) are shown. The smooth red line shows the results of a Gaussian peak fit to the Monte Carlo data (stepped black line), indicating a FWHM of 11 keV. The width is not the 1 keV width of the resonance as generated, because although all smearing effects were turned off in the simulation, the effect of the detector position resolution is always included in all simulations. This arises from the use of a polynomial fit, to obtain the excitation energy from the detected energy, for each detector pixel (or strip in the case of the LAMP array). No matter where the hit is within the pixel (or strip), the same polynomial will always be used to obtain  $E_x$ . This mimics the position resolution of the detector, as no matter the position within a pixel (or strip), only the pixel (or strip) centroid angle is known for that hit.

The effect of turning on the angular straggling of the beam in the window is shown in Fig. 9(b), and simulating all effects together in Fig. 9(c). In Fig. 9(b) the FWHM has increased from the 11 keV seen in Fig. 9(a), to 52 keV. The width of the resonance seen in Fig. 9(c) is 63 keV. This indicates that a significant contribution to the overall  $E_x$  resolution arises from the angular straggling of the beam in the window. This is supported by the results obtained at 11 – 15 and 17 MeV, as given in Tab. 2. Also listed in Tab. 2 are the

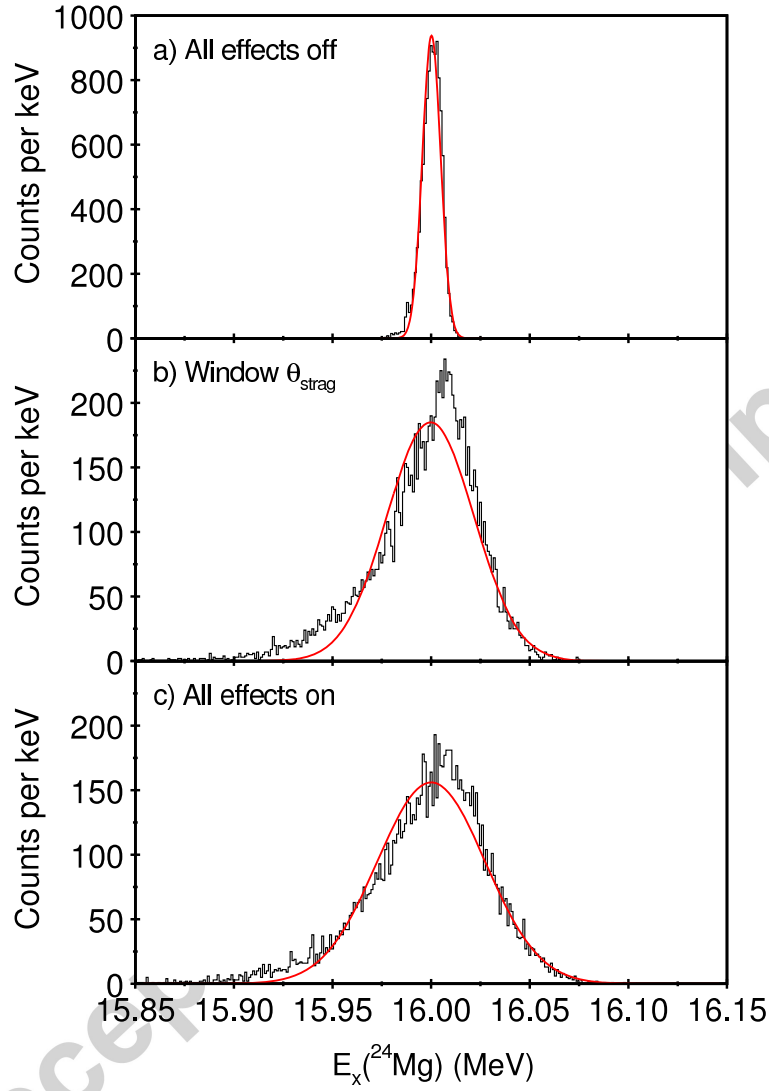


Figure 9: (Colour online) Reconstructed  $E_x$  spectra for the  $0^\circ$  DSSD of [26] obtained from REX for a state generated at  $E_x = 16$  MeV with a) all smearing effects off, b) angular straggling of the beam in the window simulated and c) all smearing effects simulated. In all panels the smooth (red) line is the result of a Gaussian peak fit to the data (stepped black line). The results are for all DSSD pixels added together.

377 contributions for each of the other smearing effects, obtained by running the  
 378 simulations multiple times, with each effect turned on individually in turn. At  
 379 all excitations it can be seen that the angular straggling of the beam in the  
 380 window dominates the overall resolution. The effect of angular straggling in  
 381 the window is to deviate the beam, so that it is no longer travelling along the  
 382 beam axis. The equations of Marion and Zimmerman [25] allow the FWHM of  
 383 the angular straggling distribution to be predicted. For a 70 MeV  $^{20}\text{Ne}$  beam  
 384 passing through a 4.8  $\mu\text{m}$  Havar<sup>®</sup> foil, the FWHM is  $1.74^\circ$ . A beam particle  
 385 scattering at an angle equal to the Half Width at Half Maximum ( $0.87^\circ$ ) would  
 386 arrive at the 17 MeV resonance (34.3 mm from the window, Fig. 4) 0.5 mm from  
 387 the beam axis, whereas at the 11 MeV resonance (270.4 mm from the window)  
 388 the deviation would be 4.1 mm, over a full DSSD strip width away. This gives  
 389 rise to the increasing resolution contribution with decreasing excitation energy,  
 390 as seen in Tab. 2. In contrast, the widths listed for the angular straggling of  
 391 the  $\alpha$ -particle in the gas are the same as those obtained with all effects turned  
 392 off, indicating that this effect is negligible.

393 The  $0^\circ$  DSSD  $E_x$  resolution, obtained with all effects off, angular straggling  
 394 of the beam in the window, and all effects turned on, is plotted as a function of  
 395 excitation energy in Fig. 10. As noted above, the contribution of the angular  
 396 straggling of the beam in the window (blue delta points and dotted line) may  
 397 be seen to be dominant at all excitation energies. It is clear, therefore, that one  
 398 way to improve the experimental excitation energy resolution would be to reduce  
 399 the window thickness, and hence the effect of angular straggling on the beam.  
 400 As a reduction in window thickness would result in a decrease in mechanical  
 401 strength, a reduction in the gas pressure may also be required. This in turn may  
 402 lead to a need to increase the detector distance, to ensure coverage of the same  
 403  $E_x$  range. Such changes are discussed below.

404 In Fig 11 the excitation energy obtained from the detected  $\alpha$ -particle energy  
 405 is shown for strip 16 (the outer strip) of the LAMP array of [26]. As in the  
 406  $0^\circ$  DSSD case (Fig. 9), these results were obtained from a simulation of a  
 407 resonance at  $E_x = 16$  MeV. In Fig. 11(a) the result obtained with all smearing

Effect	$E_x$ (MeV)						
	11	12	13	14	15	16	17
All effects off	19	17	14	12	11	11	16
Beam energy spread	29	26	23	21	20	18	21
Beam X divergence	25	22	19	16	14	13	18
Beam Y divergence	25	22	19	16	14	13	17
Beam X spot	39	34	29	24	21	19	22
Beam Y spot	21	18	15	14	12	11	16
Beam $E_{strag}$ in window	29	26	23	21	19	18	21
Beam $\theta_{strag}$ in window	125	107	92	75	63	52	49
Beam $E_{strag}$ in gas	29	26	23	21	19	19	21
Beam $\theta_{strag}$ in gas	41	33	26	21	16	14	17
Fragment $E_{strag}$ in gas	22	19	15	14	12	12	16
Fragment $\theta_{strag}$ in gas	19	17	14	13	11	11	16
Detector energy resolution	27	26	25	25	24	24	27
All effects on	142	125	105	87	73	63	56

Table 2: Predicted  $E_x$  resolution contributions (FWHM in keV) for the  $0^\circ$  DSSD of [26]. The term beam divergence represents the effect of the initial beam angular dispersion, and the term beam spot of the initial beam position dispersion. Energy and angular straggling are labelled  $E_{strag}$  and  $\theta_{strag}$ , respectively. Fitting uncertainties are  $< 1$  keV in all cases. The results shown are for all DSSD pixels together.

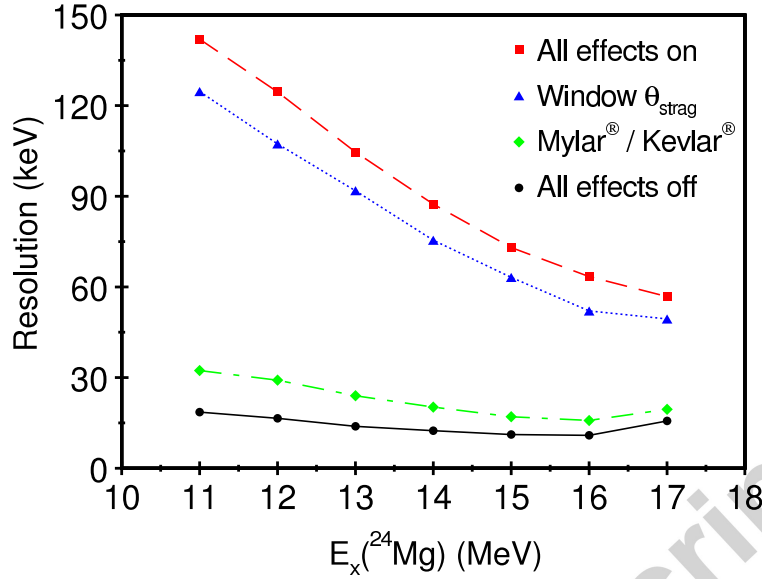


Figure 10: (Colour online) REX predicted  $E_x$  resolution (FWHM) for simulations with all smearing effects off (black circular points and solid line), angular straggling of the beam in the window (blue delta points and dotted line) and all smearing effects on (red square points and dashed line) for the  $0^\circ$  DSSD of [26], as a function of excitation energy. The green diamond points and dot-dashed line indicate the resolution contribution for a Mylar<sup>®</sup> or Kevlar<sup>®</sup> window (see Section 3.5). The results are for all DSSD pixels added together.

effects turned off is shown. The distribution is non-Gaussian, and has a width (indicated by the vertical dotted red lines) of 102 keV, with a fitting error of  $\pm 8$  keV. As described above, simulations with all effects turned off do include the detector position resolution. The width of the distribution seen in Fig. 11(a) for the LAMP array is much greater than that seen in Fig. 9(a) for the  $0^\circ$  DSSD. This is because the LAMP strips are significantly bigger than the  $(3 \times 3)$  mm pixels of the  $0^\circ$  DSSD (the outer strip of a Micron Semiconductor Ltd type YY1 detector [28] is 5 mm high and approximately 42 mm wide). This results in a much greater range of distances and scattering angles (and hence excitation energies) that can be detected in a single strip of LAMP, when compared to a pixel of the  $0^\circ$  DSSD. In Fig. 11(b) the results with the angular straggling of the beam in the window only turned on are shown. The width obtained



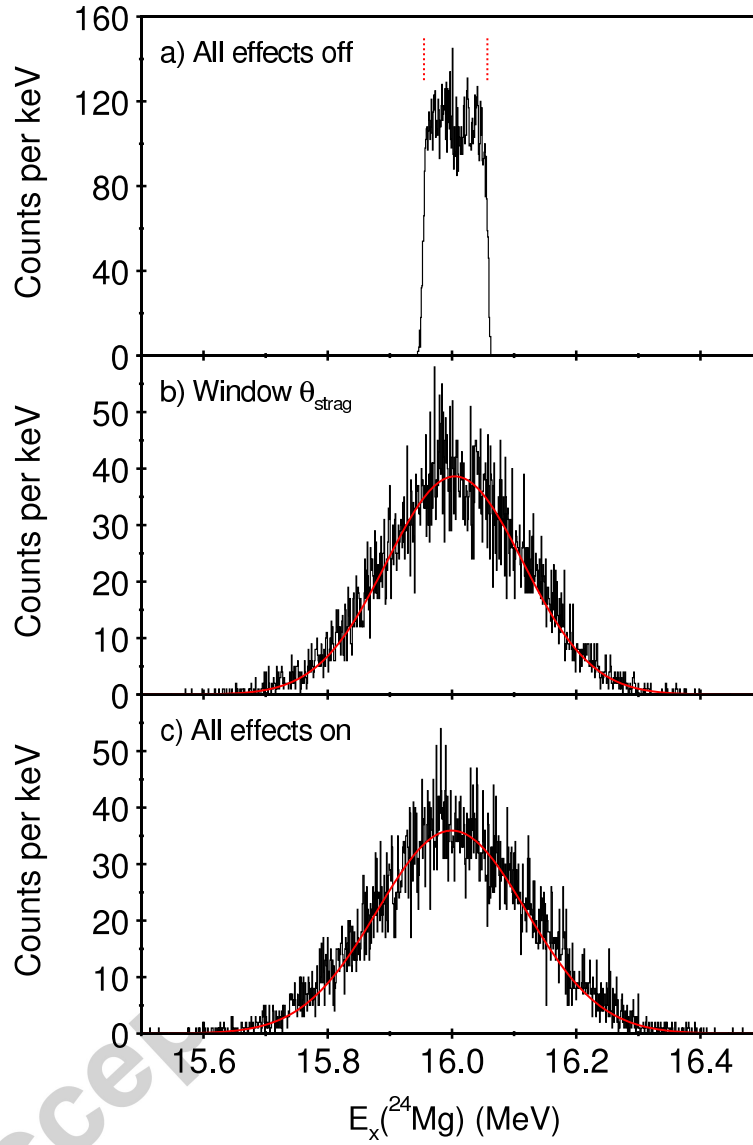


Figure 11: (Colour online) Reconstructed  $E_x$  spectra for the outer strip ( $\theta_{\text{win}} = 22.0^\circ$ ) of the LAMP array of [26] obtained from REX for a state generated at  $E_x = 16$  MeV with a) all smearing effects off, b) angular straggling of the beam in the window simulated and c) all smearing effects simulated. In a) the vertical dotted (red) lines indicate the width of the distribution. In b) and c) the smooth (red) line is the result of a Gaussian peak fit to the data.

from a Gaussian peak fit (indicated by the smooth red line) is 259 keV. As was the case for the  $0^\circ$  DSSD, the angular straggling of the beam in the window dominates the overall  $E_x$  resolution for the LAMP array, which has a FWHM of 281 keV (Fig. 11(c)) for strip 16 at  $E_x = 16$  MeV. All other strips exhibit similar behaviour, and the spectra are not presented.

In Tabs. 3, 4, 5 and 6 the contributions from all smearing effects are listed for LAMP strips 1 ( $\theta_{\text{win}} = 7.9^\circ$ ), 6 ( $\theta_{\text{win}} = 12.1^\circ$ ), 11 ( $\theta_{\text{win}} = 16.8^\circ$ ) and 16 ( $\theta_{\text{win}} = 22.0^\circ$ ), respectively. Most contributions are small, and close to those with all effects turned off. As such these smearing effects display a non-Gaussian  $E_x$  distribution (labelled “N”), due to the domination of the detector position resolution. In contrast, effects labelled “G” have a Gaussian peak shape in the reconstructed excitation energy spectrum (such as seen in Figs. 11(b) and 11(c)). These include the effect of angular straggling of the beam in the window, which in all cases dominates the overall resolution, and the overall resolution itself.

The LAMP resolutions as a function of excitation energy, obtained from simulations with all effects off, angular straggling of the beam in the window, and all effects turned on, are shown in Fig. 12, for (a) strip 1, (b) strip 6, (c) strip 11 and (d) strip 16. As seen in Fig. 10 for the  $0^\circ$  DSSD, the angular straggling of the beam in the window (blue dotted line) dominates the overall resolution (red dashed line) at all excitation energies. Reducing the window thickness is therefore again seen as a way to improve the experimental excitation energy resolution (see below).

The effect of varying the gas step size on the  $0^\circ$  DSSD excitation energy resolution is shown in Fig. 13. Resonances were generated in 1 MeV steps between 11 and 17 MeV, and gas steps of 0.1, 0.2, 0.5, 1.0, 1.5 and 2.0 mm were used. The fitting errors on the resolution values shown are  $< 1$  keV in all cases. It can be seen in Fig. 13 that at all excitations the resolutions drop between 2.0 and 1.0 mm, but then converge to a constant value (to within  $\approx 2$  keV) between 1.0 and 0.1 mm. This suggests that step sizes above 1.0 mm are too coarse to correctly sample the 4 mm FWHM of the resonances (seen in Fig. 4). The

Effect	Form	$E_x$ (MeV)					
		12	13	14	15	16	17
All effects off	N	137	112	83	63	48	36
Beam energy spread	N	142	115	90	68	50	41
Beam X divergence	N	139	117	87	61	49	39
Beam Y divergence	N	139	116	87	61	49	38
Beam X spot	G	140	127	100	76	61	48
Beam Y spot	N	139	114	87	60	49	38
Beam $E_{strag}$ in window	N	140	113	85	65	52	38
Beam $\theta_{strag}$ in window	G	343	325	255	196	155	121
Beam $E_{strag}$ in gas	N	139	114	85	69	51	40
Beam $\theta_{strag}$ in gas	N	138	112	85	60	49	37
Fragment $E_{strag}$ in gas	N	139	112	86	61	48	37
Fragment $\theta_{strag}$ in gas	N	138	111	85	63	51	40
Detector energy resolution	N	139	112	87	62	52	45
All effects on	G	385	357	280	214	168	137

Table 3: Predicted  $E_x$  resolution contributions (FWHM in keV) for strip 1 ( $\theta_{\text{win}} = 7.9^\circ$ ) of the LAMP array of [26]. The term beam divergence represents the effect of the initial beam angular dispersion, and the term beam spot of the initial beam position dispersion. Energy and angular straggling are labelled  $E_{strag}$  and  $\theta_{strag}$ , respectively. The forms G and N refer to Gaussian and non-Gaussian line shapes, with fitting uncertainties of  $< 2$  keV and  $\pm 8$  keV, respectively (see text).

Effect	Form	$E_x$ (MeV)				
		13	14	15	16	17
All effects off	N	131	115	94	74	60
Beam energy spread	N	138	119	98	79	64
Beam X divergence	N	138	120	96	76	63
Beam Y divergence	N	136	119	96	78	63
Beam X spot	G	134	128	111	92	76
Beam Y spot	N	136	117	95	80	69
Beam $E_{strag}$ in window	N	139	116	95	78	65
Beam $\theta_{strag}$ in window	G	320	304	259	217	179
Beam $E_{strag}$ in gas	N	136	118	99	79	65
Beam $\theta_{strag}$ in gas	N	140	116	96	76	61
Fragment $E_{strag}$ in gas	N	137	116	95	78	65
Fragment $\theta_{strag}$ in gas	N	134	117	95	75	62
Detector energy resolution	N	136	116	96	77	64
All effects on	G	353	337	284	237	199

Table 4: Predicted  $E_x$  resolution contributions (FWHM in keV) for strip 6 ( $\theta_{\text{win}} = 12.1^\circ$ ) of the LAMP array of [26]. The term beam divergence represents the effect of the initial beam angular dispersion, and the term beam spot of the initial beam position dispersion. Energy and angular straggling are labelled  $E_{strag}$  and  $\theta_{strag}$ , respectively. The forms G and N refer to Gaussian and non-Gaussian line shapes, with fitting uncertainties of  $< 2$  keV and  $\pm 8$  keV, respectively (see text).

Effect	Form	$E_x$ (MeV)			
		14	15	16	17
All effects off	N	123	106	94	80
Beam energy spread	N	125	111	97	84
Beam X divergence	N	125	107	95	83
Beam Y divergence	N	126	108	97	83
Beam X spot	G	124	120	110	97
Beam Y spot	N	125	110	99	86
Beam $E_{strag}$ in window	N	126	110	98	86
Beam $\theta_{strag}$ in window	G	293	283	251	218
Beam $E_{strag}$ in gas	N	124	107	95	83
Beam $\theta_{strag}$ in gas	N	129	108	98	82
Fragment $E_{strag}$ in gas	N	124	108	97	83
Fragment $\theta_{strag}$ in gas	N	125	109	95	81
Detector energy resolution	N	126	110	95	84
All effects on	G	321	311	274	239

Table 5: Predicted  $E_x$  resolution contributions (FWHM in keV) for strip 11 ( $\theta_{\text{win}} = 16.8^\circ$ ) of the LAMP array of [26]. The term beam divergence represents the effect of the initial beam angular dispersion, and the term beam spot of the initial beam position dispersion. Energy and angular straggling are labelled  $E_{strag}$  and  $\theta_{strag}$ , respectively. The forms G and N refer to Gaussian and non-Gaussian line shapes, with fitting uncertainties of  $< 2$  keV and  $\pm 8$  keV, respectively (see text).

Effect	Form	$E_x$ (MeV)			
		14	15	16	17
All effects off	N	120	113	102	90
Beam energy spread	N	123	112	104	93
Beam X divergence	N	121	111	103	91
Beam Y divergence	N	122	111	102	90
Beam X spot	G	108	113	112	102
Beam Y spot	N	122	113	103	91
Beam $E_{strag}$ in window	N	132	115	106	91
Beam $\theta_{strag}$ in window	G	252	269	259	231
Beam $E_{strag}$ in gas	N	123	113	103	91
Beam $\theta_{strag}$ in gas	N	121	111	104	90
Fragment $E_{strag}$ in gas	N	122	113	105	92
Fragment $\theta_{strag}$ in gas	N	121	112	103	91
Detector energy resolution	N	121	113	104	92
All effects on	G	280	292	281	251

Table 6: Predicted  $E_x$  resolution contributions (FWHM in keV) for strip 16 ( $\theta_{\text{win}} = 22.0^\circ$ ) of the LAMP array of [26]. The term beam divergence represents the effect of the initial beam angular dispersion, and the term beam spot of the initial beam position dispersion. Energy and angular straggling are labelled  $E_{strag}$  and  $\theta_{strag}$ , respectively. The forms G and N refer to Gaussian and non-Gaussian line shapes, with fitting uncertainties of  $< 2$  keV and  $\pm 8$  keV, respectively (see text).

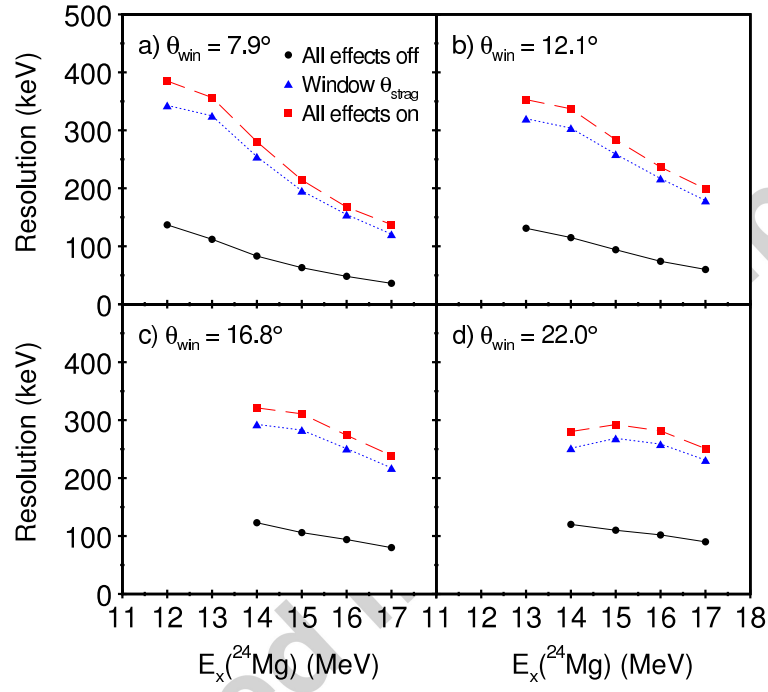


Figure 12: (Colour online) REX predicted  $E_x$  resolution (FWHM) for simulations with all smearing effects off (black circular points and solid line), angular straggling of the beam in the window (blue delta points and dotted line) and all smearing effects on (red square points and dashed line) for a) strip 1 ( $\theta_{\text{win}} = 7.9^\circ$ ), b) strip 6 ( $\theta_{\text{win}} = 12.1^\circ$ ), c) strip 11 ( $\theta_{\text{win}} = 16.8^\circ$ ) and d) strip 16 ( $\theta_{\text{win}} = 22.0^\circ$ ) of the LAMP array of [26].

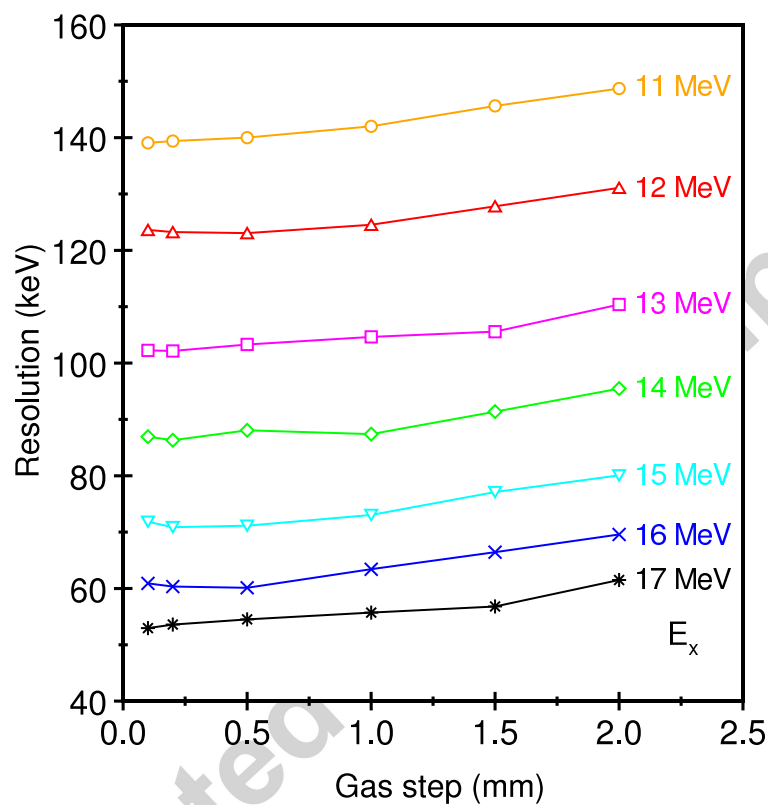


Figure 13: (Colour online) Resolution (FWHM) for the  $0^\circ$  DSSD of [26] as a function of REX gas step size, for excitation energies of 11 (orange line with circles), 12 (red line with deltas), 13 (magenta line with squares), 14 (green line with diamonds), 15 (cyan line with triangles), 16 (blue line with crosses) and 17 (black line with stars) MeV. The results are for all DSSD pixels added together.



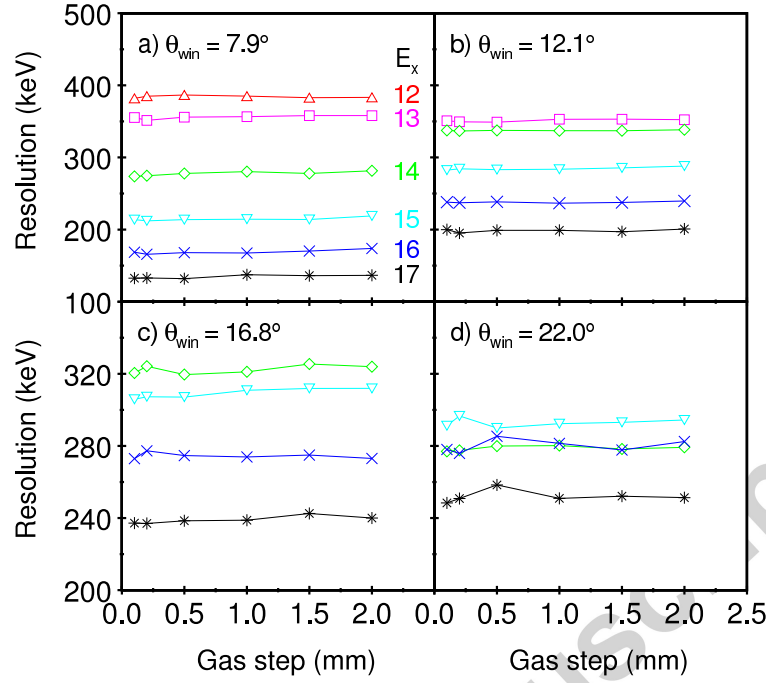


Figure 14: (Colour online) Resolution (FWHM) as a function of REX gas step size, for excitation energies of 12 (red line with deltas), 13 (magenta line with squares), 14 (green line with diamonds), 15 (cyan line with triangles), 16 (blue line with crosses) and 17 (black line with stars) MeV for a) strip 1 ( $\theta_{\text{win}} = 7.9^\circ$ ), b) strip 6 ( $\theta_{\text{win}} = 12.1^\circ$ ), c) strip 11 ( $\theta_{\text{win}} = 16.8^\circ$ ) and d) strip 16 ( $\theta_{\text{win}} = 22.0^\circ$ ) of the LAMP array of [26].

maximum resolution variation observed between 1.0 and 0.1 mm occurs at  $E_x = 16$  MeV. Here the average resolution is 61.8 keV and the variation 3.3 keV, or 5.3 %. The average variation (which gives an indication of the uncertainty of the REX resolution predictions due to the step size choice) across all excitations is 3.0 %. The results presented in Fig. 13 were obtained with a hit tolerance of 10 % of the gas step size. As for the case of detection efficiency discussed previously, repeating the simulations with a fixed hit tolerance of 0.1 mm did not produce any variations in the resolutions obtained. These results are therefore not presented.

In Fig. 14 the resolution of the LAMP array of [26] is shown as a function of the gas step size used in the simulations, for strips 1, 6, 11 and 16. The

error on each value from the peak fitting routine used to obtain the resolutions is  $\leq 2$  keV, in all cases. The resolutions are essentially independent of gas step size at all excitation energies, the maximum variation being seen for strip 16 at  $E_x = 17$  MeV (black line with stars in Fig. 14(d)). In this case the maximum variation is 10 keV, with the average resolution across all step sizes being 252 keV. This corresponds to a maximum variation in REX predicted resolution for the LAMP array of 4.0 %. Across all strips, gas step sizes and excitation energies, the average variation is 2.3 %. The dependence on gas step size seen in Fig. 13 for the  $0^\circ$  DSSD is not seen for the LAMP array in Fig. 14. This is because the LAMP resolution is much worse than that for the  $0^\circ$  DSSD, such that other effects (for example the strip position resolution) dominate. As was the case for the  $0^\circ$  DSSD, simulations in which a fixed hit tolerance of 0.1 mm was used did not alter the results shown in Fig. 14.

### 3.5. Excitation Energy

In Fig. 15(a) a  $^{24}\text{Mg}$  excitation energy spectrum, obtained from a study of the  $^{20}\text{Ne}(\alpha, \alpha_0)^{20}\text{Ne}$  reaction in standard kinematics [29], is shown. The spectrum exhibits a rich structure of states in the 12.5 – 18.5 MeV  $E_x$  range, and consists of 664 data points, each corresponding to an individual beam energy setting of the accelerator. This data has been used to investigate the accuracy of the REX resolution predictions for the  $^4\text{He}(^{20}\text{Ne}, \alpha)^{20}\text{Ne}$  data of [26]. A polynomial fit was made to the REX resolution values obtained with all smearing effects turned on, as a function of excitation energy, for the  $0^\circ$  DSSD (red dashed line in Fig. 10). The data shown in Fig. 15(a) were then convoluted with a Gaussian line shape, with a varying width taken from the polynomial fit to the REX resolution. This allows a prediction to be made of the excitation energy spectrum that should be obtained from the  $0^\circ$  DSSD of [26] (the data of [29] has a resolution of only a few keV, and is therefore a very accurate measure of the true  $^{24}\text{Mg}$  excitation energy spectrum). The result is shown by the black solid line in Fig. 15(b). Also shown (red dotted line) is the experimental  $^{24}\text{Mg}$  excitation energy spectrum obtained from the  $0^\circ$  DSSD of [26]. The agreement

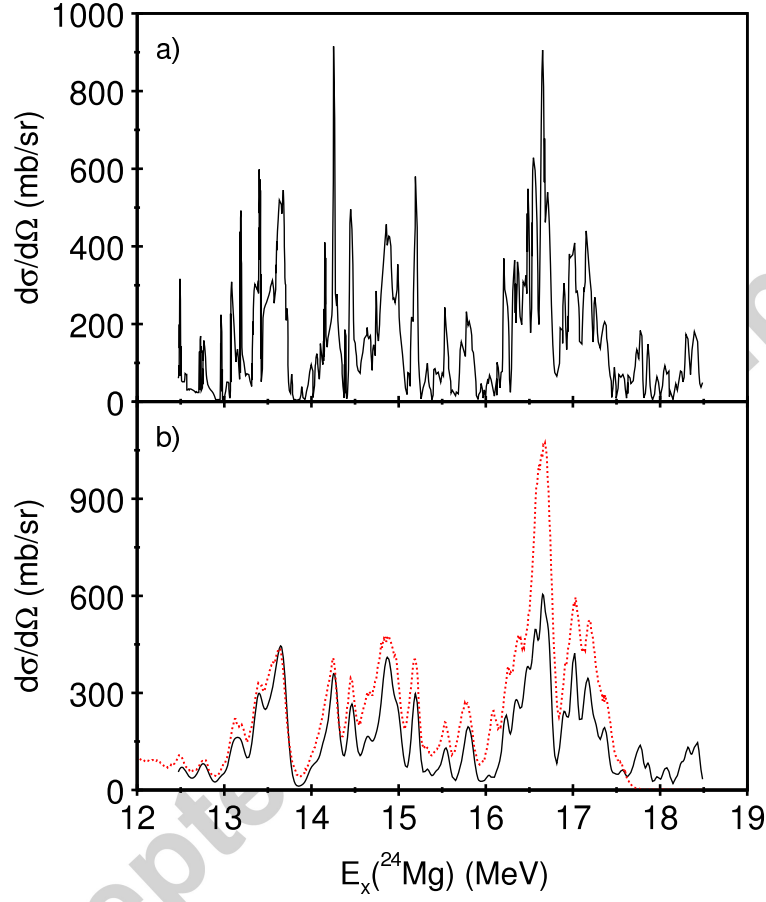


Figure 15: (Colour online) a)  $^{24}\text{Mg}$   $E_x$  spectrum from the  $^{20}\text{Ne}(\alpha, \alpha_0)^{20}\text{Ne}$  reaction [29] and b)  $^{24}\text{Mg}$   $E_x$  spectra obtained from the  $^{20}\text{Ne}(\alpha, \alpha_0)^{20}\text{Ne}$  reaction of [29] convoluted with the REX predicted resolution of [26] (black solid line) and from the  $^4\text{He}(^{20}\text{Ne}, \alpha)^{20}\text{Ne}$  reaction [26] (red dotted line).

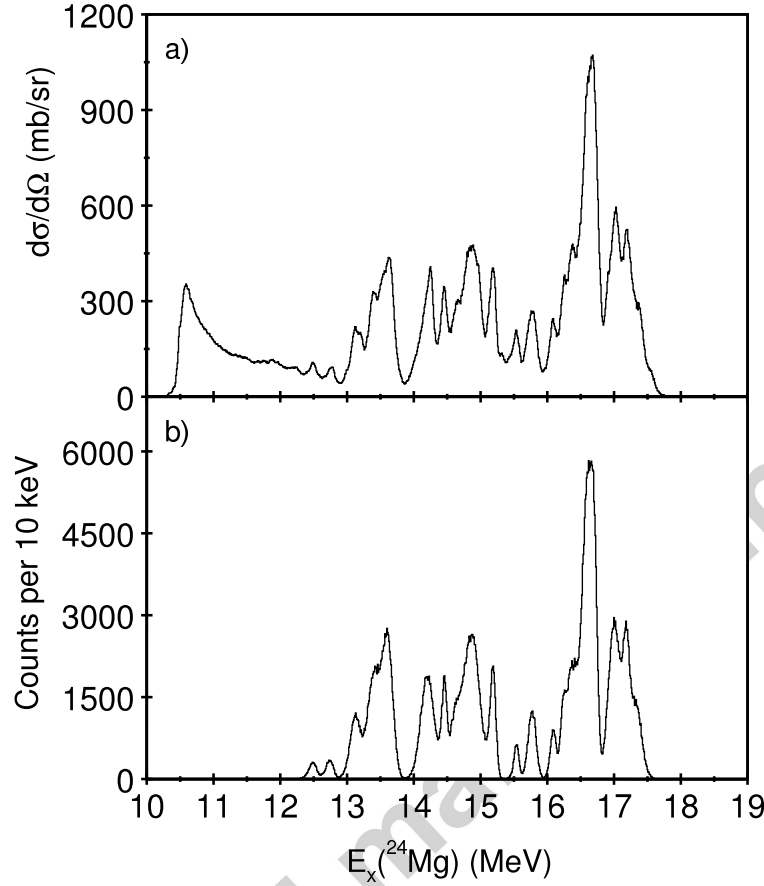


Figure 16:  $^{24}\text{Mg}$   $E_x$  spectra for the  $^4\text{He}(^{20}\text{Ne},\alpha)^{20}\text{Ne}$  reaction from the a) data of Walshe *et al.* [26] and b) REX simulation.

in terms of the general structure and widths of the features is excellent (the absolute magnitudes do vary, however, as the data of [29] was taken at a CM angle of  $168^\circ$  and that of [26] at  $180^\circ$ ). This comparison suggests that the resolutions predicted by the REX simulations are reliable.

By generating a series of resonances with varying centroids, widths and relative strengths, it is possible to reconstruct an excitation energy spectrum using REX. This is illustrated in Fig. 16. In Fig. 16(a), the experimental  $^{24}\text{Mg}$   $E_x$  spectrum obtained from the  $0^\circ$  DSSD of [26] is shown, and in Fig.16(b) a REX generated reproduction. The REX spectrum was obtained by generating 20 res-

onances between 12.5 and 17.3 MeV, with widths varying from 47 to 262 keV. The agreement between Figs. 16(a) and 16(b) is excellent, the only discrepancy being the Rutherford scattering background underlying the experimental data, which has not been included in the REX simulation. On this occasion the REX spectrum was produced after the experimental data had been analysed (the centroids, widths and relative strengths of the resonances used to generate Fig.16(b) were obtained from a fit to Fig. 16(a)). However, REX can also be used to predict the outcome of any future resonant scattering experiment, by simulating the  $E_x$  spectrum that would be obtained (using the known centroids and widths of states in the nucleus of interest, listed in compilations and data tables, for example). By altering the experimental parameters used as inputs to REX, such as the detector configuration and distance to the window, gas pressure, window thickness and window material (for example, Mylar<sup>®</sup> or Kevlar<sup>®</sup> could be substituted for Havar<sup>®</sup>, if the expected beam intensity is low), the best setup (in terms of both efficiency and resolution) can be determined.

### 3.6. Window Material

The effect of varying the window material has been investigated by performing simulations using Mylar<sup>®</sup> and Kevlar<sup>®</sup>. The window thickness used in the experiment of [26], 4.8  $\mu\text{m}$ , was used in both cases, but the beam energy altered to compensate for the differing energy loss through the different foils. For the Havar<sup>®</sup> window used in [26], the energy loss is such that the 70 MeV beam exits the foil (and enters the gas) at 50.22 MeV. Beam energies of 56.11 and 56.32 MeV were used for the Mylar<sup>®</sup> and Kevlar<sup>®</sup> simulations, respectively, to give this same energy. The  $E_x$  resolution contribution, arising from angular straggling of the beam in the window, is shown in Fig.10, for the 0° DSSD of [26]. As described in Section 3.4, the blue delta points and dotted line shows the angular straggling contribution from the Havar<sup>®</sup> window, which can be seen to dominate the overall resolution (red squares and dashed line) of the experiment. The angular straggling contributions obtained from the Mylar<sup>®</sup> and Kevlar<sup>®</sup> window simulations are identical to within 0.5 keV at all excitations, and hence an

531 averaged value for both materials is shown in Fig.10 (green diamond points and  
 532 dot-dashed line). It can be seen that the angular straggling contribution from  
 533 Mylar<sup>®</sup> and Kevlar<sup>®</sup> windows is significantly lower than that from Havar<sup>®</sup>,  
 534 indicating that Mylar<sup>®</sup> and Kevlar<sup>®</sup> provide the best choice of window mate-  
 535 rial (if the beam current is low enough to allow their use). This is supported  
 536 by the results for the LAMP array of [26]. The angular straggling contribution  
 537 for the Havar<sup>®</sup> window of [26] is shown by the blue delta points and dotted  
 538 line in Fig.12 (described in Section 3.4), and again can be seen to dominate the  
 539 overall experimental resolution. The results for Mylar<sup>®</sup> and Kevlar<sup>®</sup> windows  
 540 have been found to be indistinguishable from those obtained with all smearing  
 541 effects turned off (black circular points and solid line in Fig.12), and are not  
 542 shown. This suggests that the contributions from angular straggling of the beam  
 543 in these window materials is much smaller than those arising from the LAMP  
 544 strip position resolution.

545 The difference in angular straggling contributions from Mylar<sup>®</sup>, Kevlar<sup>®</sup>  
 546 and Havar<sup>®</sup> result from the different compositions of the materials. Mylar<sup>®</sup>  
 547 (composed of C, H and O) and Kevlar<sup>®</sup> (composed of C, H, O and N) have much  
 548 lower average masses, charges and densities than Havar<sup>®</sup> (composed mainly of  
 549 Co, Cr, Ni and Fe). Because Havar<sup>®</sup> consists almost entirely of metals, it  
 550 is both mechanically strong and an excellent conductor. This allows the heat  
 551 arising from the energy loss of the beam as it passes through the foil to be easily  
 552 dissipated. In contrast, Mylar<sup>®</sup> and Kevlar<sup>®</sup> are both insulators, and will likely  
 553 melt under exposure to high beam currents. In a radioactive beam experiment,  
 554 where the beam currents are typically low, it may be possible to use Mylar<sup>®</sup> or  
 555 Kevlar<sup>®</sup> windows without risking a catastrophic failure due to melting (in the  
 556 experiment of [2] a 2.5  $\mu\text{m}$  Mylar<sup>®</sup> window was used with a beam intensity of  
 557  $\sim 2 \times 10^6$  particles per second, although the gas pressure was only 150 mb).  
 558 For higher beam intensities a Havar<sup>®</sup> window may well have to be used, or at  
 559 the very least Mylar<sup>®</sup> or Kevlar<sup>®</sup> with a thin aluminium coating.

560 To illustrate the advantages of using a thinner and lighter window, a sim-  
 561 ulation has been performed for the  $^4\text{He}(^{20}\text{Ne},\alpha)^{20}\text{Ne}$  reaction of [26], in which

Mylar<sup>®</sup> was used instead of Havar<sup>®</sup>. The window thickness was reduced (by  
 a factor of two) to 2.4  $\mu\text{m}$ , and the gas pressure halved (to 270 torr) to reflect  
 the use of a thinner (and weaker) window. To account for the lower energy  
 loss through the Mylar<sup>®</sup>, a beam energy of 53.20 MeV was used. This gives  
 the same 50.22 MeV into the gas as the setup of [26]. As the resonances will  
 be spread further into the chamber due to the use of a lower gas pressure, the  
 LAMP and 0° DSSD distances were increased to 535 and 740 mm, respectively.  
 These settings result in the same excitation energy range being covered by each  
 detector in the two configurations, as seen in Fig. 17. Here the efficiency profiles  
 are shown for both the experimental setup of [26] (previously shown in Fig. 5)  
 (black solid lines) and for the new simulation (blue dotted lines). In the case of  
 the 0° DSSD (Fig. 17(a)) the efficiency is seen to drop by a factor of 4.4, a result  
 of the approximately doubling of the window to DSSD distance (from 360 to 740  
 mm). As the distances of the resonances into the chamber have also doubled  
 (the  $E_x = 17$  MeV resonance moves from 34.3 (Sec. 3.2) to 68.3 mm, and that  
 at  $E_x = 11$  MeV from 270.4 to 540.5 mm) the resonance to DSSD distances have  
 also increased. For example, at  $E_x = 17$  MeV, the resonance to DSSD distance  
 ( $R_r$ ) is  $360.0 - 34.3 = 325.7$  mm at 540 torr and  $740.0 - 68.3 \text{ mm} = 671.7$   
 mm at 270 torr, a ratio of  $671.7/325.7 = 2.1$ . As the solid angle covered by the  
 DSSD with respect to the resonance point depends on  $1/R_r^2$ , a change in  $R_r$  by  
 a factor of 2.1 leads to a decrease in solid angle by a factor of  $2.1^2 = 4.4$ . Hence  
 the drop in efficiency seen for the 0° DSSD in Fig. 17(a) results entirely from  
 the changing geometry of the two experimental setups simulated. In the case of  
 the LAMP array (Fig. 17(b)) the efficiency profile appears narrower, and the  
 peak shifted towards lower excitation, in the new simulation. This again results  
 from the increased resonance to detector distance, which leads to a reduction  
 in the angular range covered by the array. For example, at 284 mm the centre  
 of the inner strip is at  $\theta_{\text{win}} = 7.9^\circ$ , which reduces to  $4.2^\circ$  at 535 mm. For the  
 outer strip the angle changes from  $22.0^\circ$  at 284 mm to  $10.9^\circ$  at 535 mm. It is  
 this narrowing of the angular range of the LAMP array at 535 mm that leads  
 to the corresponding narrowing of the efficiency profile. Despite this, it can be

seen in Fig. 17 that the excitation energy range covered is the same for both experimental setups.

In Figs. 18 and 19 the excitation energy resolution is shown for the experimental setup of [26] (black solid line) (previously shown in Figs. 10 and 12) and for the new simulation (blue dotted line). For both the  $0^\circ$  DSSD (Fig. 18) and LAMP array (Fig. 19) the improvement in resolution is clear, and arises from the reduction in angular straggling of the beam in the window in the proposed improved setup. In the case of the  $0^\circ$  DSSD (Fig. 18) the resolution reduces to approximately 30 keV at all excitations, a decrease by a factor of 4.1 at  $E_x = 11$  MeV and 2.0 at 17 MeV. For the 4 strips of the LAMP array shown in Fig. 19, the resolution drops by a factor of a minimum of 2.3 (Strip 1 at  $E_x = 12$  MeV and Strip 16 at  $E_x = 14$  MeV) and a maximum of 4.2 (Strip 11 at  $E_x = 17$  MeV). It is clear, therefore, that unless limited by low beam intensity (and hence low counting statistics) it would, in general, be better to use the thinnest Mylar<sup>®</sup> or Kevlar<sup>®</sup> window possible in future work. Although this would require lowering the gas pressure and pushing the detectors further from the window (when compared to a measurement using a thick Havar<sup>®</sup> foil), the decrease in efficiency would be compensated by the much greater experimental resolution, and hence quality of the data obtained.

### 3.7. Angular Distribution

In both the  $^4\text{He}(^6\text{He},\alpha)^6\text{He}$  measurement of [2], and the  $^4\text{He}(^{10}\text{Be},\alpha)^{10}\text{Be}$  reaction studied in [11], spin information was obtained for the resonances observed following a study of the  $\alpha$ -particle angular distributions. These may be simulated in REX, an example for the  $^4\text{He}(^{20}\text{Ne},\alpha)^{20}\text{Ne}$  reaction being shown in Fig. 20. Here the detected  $\alpha$ -particle energy has been plotted against angle with respect to the window (which has been smeared randomly within the range of the pixel or strip hit in the event). In Fig. 20(a) the angular distribution is shown for the experimental data of [26]. The data observed between  $0^\circ$  and  $5.8^\circ$  correspond to that obtained from the  $0^\circ$  DSSD, and that between  $7.5^\circ$  and  $22.5^\circ$  to the LAMP array. A series of loci can be seen, each corresponding to



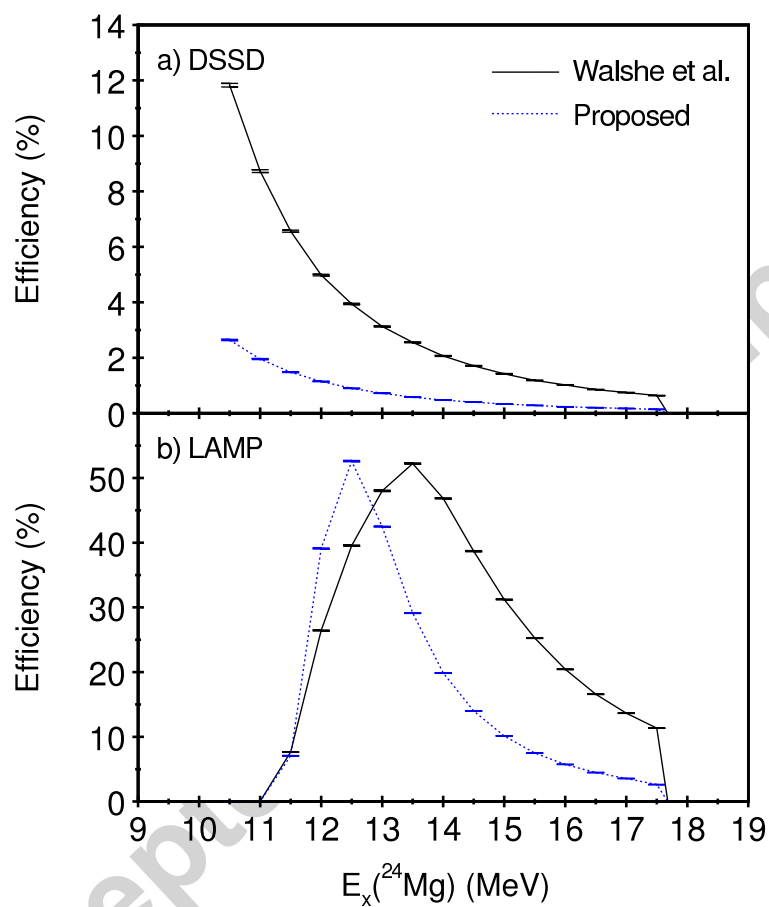


Figure 17: (Colour online) Efficiency profiles for the experiment of [26] (black solid lines) and proposed improved setup (see text) (blue dotted lines) for the a)  $0^\circ$  DSSD and b) LAMP array.

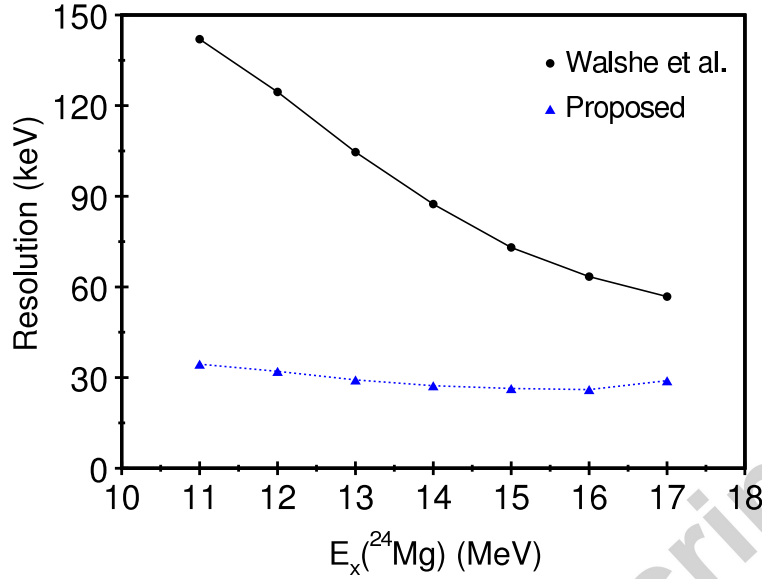


Figure 18: (Colour online) REX predicted  $E_x$  resolution (FWHM) for the  $0^\circ$  DSSD of [26] (black solid line) and proposed improved setup (see text) (blue dotted line).

one of the individual resonances seen in Fig. 16(a). In Fig. 20(b) a REX generated version of the same angular distribution is shown. This was obtained from the same simulation used to produce the excitation energy spectrum shown in Fig.16(b). In general, the agreement in coverage between Figs. 20(a) and 20(b) is excellent, with the only discrepancy being in the low energy ( $E_d < 10$  MeV) region. This arises because in the experimental data Rutherford scattering is observed in the DSSD, and noise seen in the LAMP array. Neither of these effects are included in the REX simulation. The REX spectrum shown in Fig. 20(b) was produced in a simulation in which a uniform angular distribution was used for the scattering. This results in an intensity pattern that varies smoothly with angle, and which reflects the detection efficiency of the experimental setup. This is in contrast to the experimental data (Fig. 20(a)), in which much greater variations in intensity can be observed in the loci as a function of angle, a result of the spins of the resonances. This difference can be clearly seen in the regions surrounding the solid black line in both panels of Fig. 20, which represents the

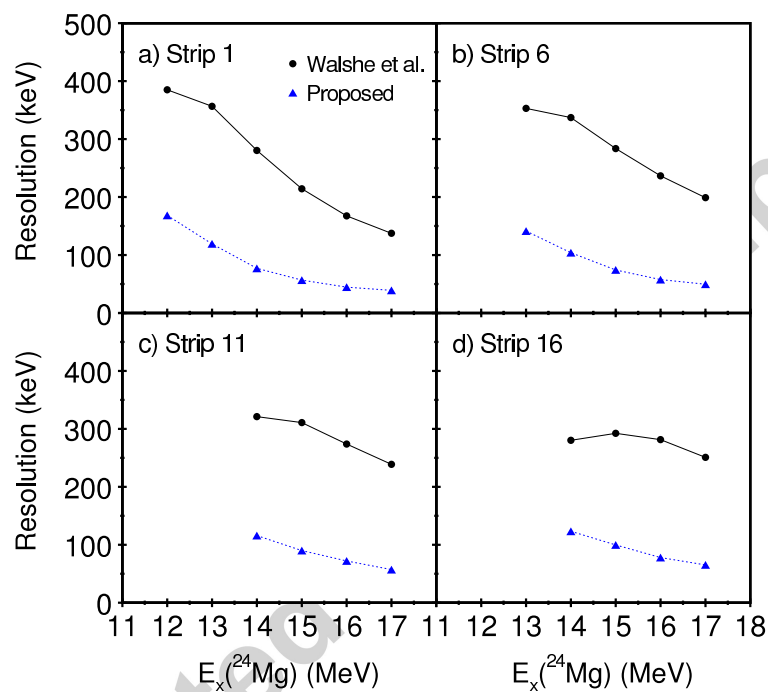


Figure 19: (Colour online) REX predicted  $E_x$  resolution (FWHM) for strips a) 1, b) 6, c) 11 and d) 16 of the LAMP array of [26] (black solid line) and proposed improved setup (see text) (blue dotted line).

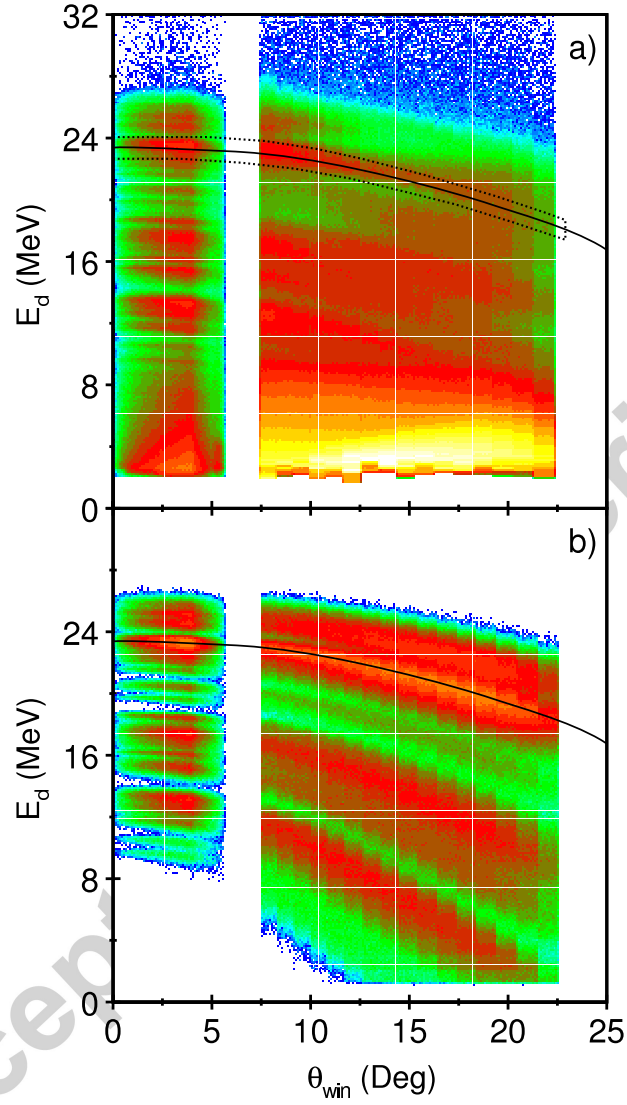


Figure 20: (Colour online) Detected energy against angle for a) the data of [26] and b) a REX simulation. In both panels the solid black line shows a REX simulation of a resonance at  $E_x = 16.64$  MeV, with all smearing effects off. The dotted line in a) indicates the window used to select events (see text).

638 result of a simulation for a single resonance at  $E_x = 16.64$  MeV, obtained from  
 639 REX with all smearing effects turned off. The intensity in the region of this line  
 640 in Fig. 20(b) varies smoothly with angle, whilst in Fig. 20(a) the experimental  
 641 data can be seen exhibit much more variation.

642 In Fig. 21 the projection of the experimental angular distribution seen within  
 643 the dotted window in Fig. 20(a) is shown. Also shown are the results of REX  
 644 simulations for a single  $E_x = 16.64$  MeV resonance, obtained with differing  
 645 Legendre polynomial ( $P_L$ ) angular distributions for the scattering reaction. In  
 646 Fig. 21(a) the results of a simulation with  $L = 3$  are shown, in Fig. 21(b) the  
 647 results for  $L = 4$  and in Fig. 21(c)  $L = 5$ . No single  $L$  value can reproduce  
 648 the data, although a simple sum of 72 %  $L = 3$  and 28 %  $L = 5$  (without  
 649 any interference included) does provide a reasonable description, as seen in  
 650 Fig. 21(d). Performing additional simulations for all of the resonances seen in  
 651 Fig. 20(a) would allow the spins to be investigated and the dominant  $L$  values  
 652 determined.

#### 653 4. Summary

654 A Monte Carlo code (REX) has been developed in order to simulate thick  
 655 gas target resonant scattering experiments. After simulating the effects of the  
 656 beam energy spread from the accelerator, beam divergence, beam spot size,  
 657 beam offset from the centre of the window and the window itself, the beam is  
 658 tracked in steps through the gas. After each step the effects of energy loss, energy  
 659 straggling and angular straggling on the beam energy, position and trajectory  
 660 are determined. Once the interaction point has been reached, the scattering  
 661 reaction is simulated, and the outgoing particles then tracked in steps in a  
 662 similar manner to the beam. For events in which a particle hits a detector, the  
 663 effects of detector energy and position resolution are simulated, and the event  
 664 written to a file for analysis.

665 Simulations of the  ${}^4\text{He}({}^{20}\text{Ne},\alpha){}^{20}\text{Ne}$  reaction have been performed, the ef-  
 666 ficiency and resolution investigated, and the excitation energy spectrum and

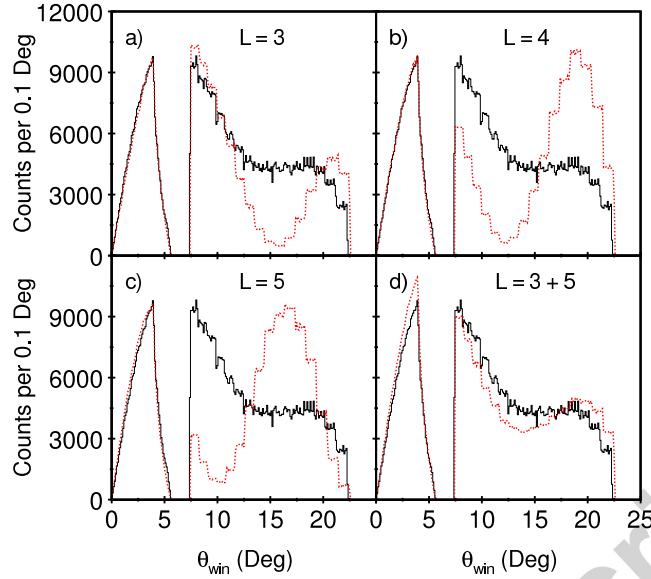


Figure 21: (Colour online) Angular distribution for the resonance at  $E_x = 16.64$  MeV in the data of [26] (black solid line) overlaid with the REX prediction (red dotted line) for a)  $L = 3$ , b)  $L = 4$  and c)  $L = 5$ . In d) the weighted sum of  $L = 3$  (72 %) and 5 (28 %) is shown.

angular distribution reproduced. Comparisons to the experimental results of a measurement performed at GANIL [26] indicate the results obtained from REX are reliable. The excitation energy resolution is found to be dominated by angular straggling in the window, indicating that the window thickness and material (and hence gas pressure and detector distances) must be considered carefully in the planning of future experiments.

## 5. Acknowledgements

This work was funded by the United Kingdom Science and Technology Facilities Council (NC) and the School of Physics and Astronomy, University of Birmingham, UK (JW).

- [1] K.P. Artemov, O.P. Belyanin, A.L. Vetoshkin, R. Wolskj, M.S. Golokov, V.Z. Gol'dberg, M. Madeja, V.V. Pankratov, I.N. Serikov, V.A. Timofeev, V.N. Shadrin and J. Szmider, *Sov. J. Nucl. Phys.* 52(3) (1990) 408.

- [2] M. Freer, E. Casarejos, L. Achouri, C. Angulo, N.I. Ashwood, N. Curtis, P. Demaret, C. Harlin, B. Laurent, M. Milin, N.A. Orr, D. Price, R. Raabe, N. Soić and V.A. Ziman, Phys. Rev. Lett. 96 (2006) 042501.
- [3] Changbo Fu, V.Z. Goldberg, G.V. Rogachev, G. Tabacaru, G.G. Chubar-ian, B. Skorodumov, M. McCleskey, Y. Zhai, T. Al-Abdullah, L. Trache and R.E. Tribble, Phys. Rev. C77 (2008) 064314.
- [4] N.I. Ashwood, M. Freer, N.L. Achouri, T.R. Bloxham, W.N. Catford, N. Curtis, P.J. Haigh, C.W. Harlin, N.P. Patterson, D.L. Price, N. Soić and J.S. Thomas, J. Phys. G: Nucl. Part. Phys. 36 (2009) 055105.
- [5] T. Lönnroth, M. Norrby, V.Z. Goldberg, G.V. Rogachev, M.S. Golovkov, K.-M. Källman, M. Lattuada, S.V. Perov, S. Romano, B.B. Skorodumov, G.P. Tiourin, W.H. Trzaska, A. Tumino and A.N. Vorontsov, Eur. Phys. J. A46 (2010) 5.
- [6] H. Yamaguchi, T. Hashimoto, S. Hayakawa, D.N. Binh, D. Kahl, S. Kubono, Y. Wakabayashi, T. Kawabata and T. Teranishi, Phys. Rev. C83 (2011) 034306.
- [7] M. Freer, N.I. Ashwood, N. Curtis, A. Di Pietro, P. Figuera, M. Fisichella, L. Grassi, D. Jelavić Malenica, Tz. Kokalova, M. Koncul, T. Mijatović, M. Milin, L. Prepolec, V. Scuderi, N. Skukan, N. Soić, S. Szilner, V. Tokić, D. Torresi and C. Wheldon, Phys. Rev. C84 (2011) 034317.
- [8] M. Norrby, T. Lönnroth, V.Z. Goldberg, G.V. Rogachev, M.S. Golovkov, K.-M. Källman, M. Lattuada, S.V. Perov, S. Romano, B.B. Skorodumov, G.P. Tiourin, W.H. Trzaska, A. Tumino and A.N. Vorontsov, Eur. Phys. J. A47 (2011) 96.
- [9] A. Di Pietro, D. Torresi, M. Zadro, L. Cosentino, C. Ducoin, P. Figuera, M. Fisichella, M. Lattuada, C. Maiolino, A. Musumarra, M. Papa, M.G. Pellegriti, M. Rovituso, D. Santonocito, G. Scalia, V. Scuderi and E. Strano, J. Phys. Conf. Series, 366 (2012) 012013.

- [10] H. Yamaguchi, D. Kahl, Y. Wakabayashi, S. Kubono, T. Hashimoto, S. Hayakawa, T. Kawabata, N. Iwasa, T. Teranishi, Y.K. Kwon, D.N. Binh, L.H. Khiem and N.N. Duy, Phys. Rev. C87 (2013) 034303.
- [11] M. Freer, J.D. Malcolm, N.L. Achouri, N.I. Ashwood, D.W. Bardayan, S.M. Brown, W.N. Catford, K.A. Chipps, J. Cizewski, N. Curtis, K.L. Jones, T. Munoz-Britton, S.D. Pain, N. Soić, C. Wheldon, G.L. Wilson and V.A. Ziman, Phys. Rev. C90 (2014) 054324.
- [12] M.L. Avila, G.V. Rogachev, V.Z. Goldberg, E.D. Johnson, K.W. Kemper, Yu. M. Tchuvil'sky and A.S. Volya, Phys. Rev. C90 (2014) 024327.
- [13] S. Agostinelli et al., Nucl. Instrum. Meth. A 506 (2003) 250.
- [14] N. Curtis, N.M. Clarke, B.R. Fulton, S.J. Hall, M.J. Leddy, A. St.J. Murphy, J.S. Pople, R.P. Ward, W.N. Catford, G.J. Gyapong, S.M. Singer, S.P.G. Chappell, S.P. Fox, C.D. Jones, D.L. Watson, W.D.M. Rae and P.M. Simmons, Phys. Rev. C51 (1995) 1554.
- [15] C. Arpesella, E. Bellotti, C. Broggin, P. Corvisiero, S. Fubini, G. Gervino, U. Greife, C. Gustavino, M. Junker, A. Lanza, P. Prati, C. Rolfs, D. Zahnow and S. Zavatarelli, Nucl. Instrum. Meth. A 360 (1995) 607.
- [16] M.C. Morone, G. Oliviero, L. Campajola, A. D'Onofrio, L. Gialanella, M. La Commara, V. Roca, M. Romano, M. Romoli, F. Terrasi, R. Barnà, D. De Pasquale, M. Aliotta, S. Cherubini, M. Lattuada, S. Romano and C. Spitaleri, Nucl. Instrum. Meth. A 419 (1998) 167.
- [17] L. Weissman, J. Van. Roosbroeck, K. Kruglov, A. Andreyev, B. Bruyneel, S. Franchoo, M. Huyse, Y. Kudryavtsev, W.F. Mueller, R. Raabe, I. Reusen, P. Van Duppen and L. Vermeeren, Nucl. Instrum. Meth. A 423 (1999) 328.
- [18] C. Dörr and H.V. Klapdor-Kleingrothaus, Nucl. Instrum. Meth. A 513 (2003) 596.



- [19] R.P. Schmitt, L. Cooke, G. Derrig, D. Fabris, B. Hurst, J.B. Natowitz, G. Nebbia, D. O’Kelly, B.K. Srivastava, W. Turmel, D. Utley, H. Utsunomiya and R. Wada, Nucl. Instrum. Meth. A 354 (1995) 487.
- [20] J. Ljungvall, M. Palacz and J. Nyberg, Nucl. Instrum. Meth. A 528 (2004) 741.
- [21] M.A. Ludington and R.G. Helmer, Nucl. Instrum. Meth. A 446 (2000) 506.
- [22] R.G. Helmer, J.C. Hardy, V.E. Jacob, M. Sanchez-Vega, R.G. Neilson and J. Nelson, Nucl. Instrum. Meth. A 511 (2003) 360.
- [23] Computer program DEDX (University of Birmingham, UK) unpublished. Based on computer program SPAR, T.W. Armstrong and K.C. Chandler, ORNL-4869 (Oak Ridge National Laboratory, US) 1973 and T.W. Armstrong and K.C. Chandler, Nucl. Instrum. Meth. 113 (1973) 313.
- [24] N.M. Clarke, Nucl. Instrum. Meth. 96 (1971) 497.
- [25] J.B. Marion and B.A. Zimmerman, Nucl. Instrum. Meth. 51 (1967) 93.
- [26] J. Walshe, M. Freer, C. Wheldon, L.N. Achouri, N.I. Ashwood, W.N. Catford, I.C. Celik, N. Curtis, F. Delaunay, B. Fernández-Domínguez, L. Grassi, Tz. Kokalova, M. Marqués, N.A. Orr, L. Prepolec, N. Soić and V. Tokić, J. Phys. Conf. Series, 569 (2014) 012052
- [27] Micron Semiconductor Ltd, 1 Royal Buildings, Marlborough Road, Lancing Business Park, Lancing, Sussex, BN15 8SJ, United Kingdom.
- [28] T. Davinson, W. Bradfield-Smith, S. Cherubini, A. DiPietro, W. Galister, A.M. Laird, P. Leleux, A. Ninane, A.N. Ostrowski, A.C. Shotter, J. Vervier and P.J. Woods, Nucl. Instrum. Meth. A 454 (2000) 350.
- [29] R. Abegg and C.A. Davis, Phys. Rev. C43 (1991) 2523.